ACS APPLIED ENERGY MATERIALS

Open Access

This article is licensed under CC-BY 4.0

www.acsaem.org

Article

Investigation of In Situ Cross-linked Polyacrylic Acid-PEG Binder for Si-dominant Anodes in Lithium-Ion Full Cells

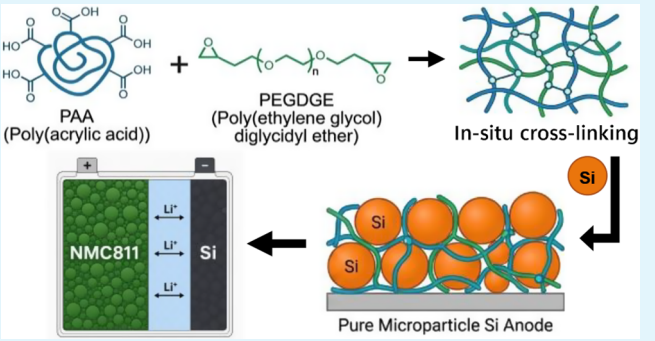
Gabriele Kloker,* Dragoljub Vrankovic, Nikhil Arya, and Montaha Anjass*

Cite This: *ACS Appl. Energy Mater.* 2026, 9, 10674−10688

Read Online

ACCESS | Metrics & More | Article Recommendations | Supporting Information

ABSTRACT: Silicon (Si) is a highly promising anode material for lithium-ion batteries due to its high theoretical capacity. However, its practical use is limited by significant volume changes and resulting degradation during cycling. To enhance the mechanical stability of the Si anode, polyacrylic acid (PAA), a prominently used binder, was cross-linked in situ during electrode fabrication with the bifunctional and ion-conducting poly(ethylene glycol) diglycidyl ether (PEGDGE). The resulting binder architecture was designed to strengthen the binder network while accommodating substantial volume changes during cycling. The epoxide-containing PEGDGE was incorporated into the binder or as functionalization on the silicon particles. The resulting pure silicon anodes exhibited strong adhesion and cohesion, contributing to improved electrochemical performance, as determined by cyclic voltammetry and long-term galvanostatic cycling (up to 150 cycles at 1C until state of health 80%). Post-mortem analysis revealed well-maintained electrode morphology and the formation of a LiF-rich, stable solid electrolyte interphase (SEI) as identified by SEM and XPS, respectively. These results highlight the potential of the cross-linker to enhance the structural integrity and the electrochemical performance of silicon anodes.

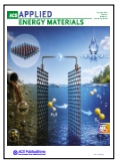


KEYWORDS: *silicon-dominant anode, full cell, in situ cross-linking, polyacrylic acid, poly(ethylene glycol) diglycidyl ether (PEGDGE), PAA-PEG binder, silicon microparticles*

INTRODUCTION

Lithium-ion batteries (LIBs) play a pivotal role in advancing clean energy technology, particularly in the mobility sector, where sustainable energy solutions are urgently needed. As the demand for higher energy densities grows, the traditionally used graphite anodes are approaching their capacity limit, and materials with higher capacities are needed. Silicon (Si), with its high theoretical capacity of >3500 mAh g^{-1} at room temperature and a low discharge potential of about 0.37 V vs lithium (Li) metal, has emerged as a highly promising candidate for next-generation anode materials. Additionally, Si is an abundant, environmentally friendly, and low-cost element.[1−5] Nevertheless, its use in current LIB applications remains limited due to challenges associated with its Li storage mechanism. During alloying with lithium, Si undergoes extreme volume changes of more than 300%, which leads to electrode and particle cracking, loss of electrical contact, and excessive solid electrolyte interphase (SEI) growth because of continuous exposure of the fresh Si surface to electrolyte, leading to active Li loss.[1,2,5−7] Additional Li loss can occur due to Li trapping within the particles.[8−10] To overcome these issues and enable the use of Si in industrial-scale cells, three key strategies are widely adopted: (i) the design of nanostructured Si, integrated into a carbon matrix, (ii) the use of electrolyte(s) with suitable additives, or (iii) the development of new binder systems capable of accommodating Si volume expansion.[2,5−7,11−15] While each strategy has its benefits and drawbacks, it is important to consider their interplay and targeted application. In many studies, Si nanoparticles (SiNPs) are used in a small ratio with graphite, as this approach prevents particle cracking.[7,16−18] However, the high surface area leading to strong electrolyte degradation as well as the difficult processing resulting in electrodes with low density[16] hinders potential application of these SiNPs in graphite anodes. Si microparticles (SiMPs) are the cost-effective opposite with higher tap density of the Si powder, reduced surface area, and therefore reduced loss of active Li due to side reactions. Their internal strain and following particle fracture upon cycling make their application challenging as well.[19]

Received: May 9, 2026
Revised: August 2, 2026
Accepted: August 4, 2026
Published: August 14, 2026



Downloaded from pubs.acs.org/aaemcq/article-pdf/9/16/10674/6543599/ae-2026-015488.pdf by KIT BIBLIOTHEK user on 02 November 2026

Therefore, an important aspect is the limitation of capacity to minimize volume change[20] and the design of suitable binder systems, which are robust and at the same time flexible enough to maintain electrode integrity. Many different variations have been published, coming from more commonly used linear binders like polyacrylic acid (PAA) to cross-linked binders and even systems with self-healing ability.[21−29] However, since binders are electrochemically inactive materials and are used in relatively small quantities within the cell, their suitability for large-scale industrial application depends on being cost-effective and easily processable in an aqueous environment.[27−33] PAA, with abundant functional groups—carboxyl groups (COOH)—does not only allow good interaction with the Si surface and its silanol (Si–O–H) groups, but it also enables versatile interactions with cross-linkers while itself providing great properties as a binder for Si anodes. Furthermore, the chemical interaction as well as the polymer conformation can be changed by partial neutralization of the PAA carboxyl groups, which also influences the homogeneity of polymer distribution around the particles.[34−39] Providing the option for cross-linking, the respective additive acting as a cross-linker needs to be chosen wisely to add desired properties. Ideally, the cross-linker is incorporated via in situ cross-linking between PAA and the cross-linker as shown in literature[40,41] to create a drop-in solution to the existing slurry preparation without extensive binder synthesis. As reported in previous studies,[21,22,24,28,29,42] strong adhesion and cohesion are important binder properties, and elasticity also plays a key role in accommodating the large volume changes of Si during cycling. The use of polar polymers with functional groups enhances binder adhesion to Si and thus improves the integrity of the anode. By creating strong binder networks with cross-linking, the Si particles are kept in place. Achieving an optimal balance between mechanical stability (modulus) and elasticity is essential.[24,28,30,43] Additionally, the electrochemical properties of the binder and cross-linker are important, as they influence the electronic and ionic conductivity of the electrode. Also, electrolyte uptake plays a role as it can have a detrimental impact on the binder modulus. Lastly, the binder also influences SEI formation, as it surrounds the active material. As this passivation layer is mostly electronically insulating and ionically conductive, these properties should be considered.[44] A combination of binder and cross-linker can merge beneficial properties of both components and may even produce synergistic effects.[24,28,30] As already known from solid polymer electrolytes, polyethylene oxide (PEO) and polyethylene glycol (PEG) exhibit both elasticity and Li-ion conductivity.[45] Since these properties are expected to be beneficial for Si anodes as well, some studies started to incorporate them in the Si anode with promising results.[29,46−48] Implementation of PEG as a bifunctional oligomer offers easier ways of reaction and can be achieved via ring-opening polymerization (ROP), as already shown in solid electrolyte studies.[49,50] Therefore, poly(ethylene glycol) diglycidyl ether (PEGDGE) as a cross-linker offers not only a desired combination between a soft elastic cross-linker and rigid polymer chains of PAA but also potentially easy cross-linking via epoxide ring opening and reaction with the carboxyl groups of PAA via esterification. Based on this idea, PEGDGE was implemented not only as a cross-linker in acidic PAA (Li_0PAA) and in 30% neutralized PAA ($Li_{0.3}$PAA) but also as a functionalization group on the Si surface to study its impact on the Si anode.

EXPERIMENTAL SETION

Binder and Electrode Preparation

The binder and electrode preparation were conducted under ambient conditions. All reagent-grade chemicals were purchased from Sigma-Aldrich and were used without further purification. The weight percentages (wt %) of electrode components were given based on the dry electrode.

Preparation of PAA-PEG and Partially Neutralized PAA-PEG. A 10 wt % PAA solution was prepared by dissolving PAA powder (average $M_w \sim 450{,}000$ g mol^{-1}) in deionized water using a magnetic stirrer. 1 mol L^{-1} lithium hydroxide (LiOH) solution was used for partial neutralization of PAA to 30% ($Li_{0.3}$PAA). The necessary amount of LiOH solution was calculated depending on the PAA amount; for example, 12 mL of LiOH solution was added to 24 g of PAA solution used for 1/10 cross-linked $Li_{0.3}$PAA binder. The solution was left for at least 1 h to reach equilibrium, and the neutralization degree was checked via pH measurement compared to a titration-based neutralization curve.

PEGDGE (average $M_w \sim 500$ g mol^{-1}) was used as a cross-linker. The amount of PAA solution was determined by the cross-linking ratio with PEGDGE to result in a total of 8% binder in the electrode (e.g., 24 g for 1/10 cross-linking ratio). The amount of PEGDGE added to the binder solution was calculated based on the number of functional groups of both components to achieve the desired cross-linking ratio. As acidic PAA provides one functional group per unit, the available functional groups can be calculated with $M_{(unit)}/M_w$. PEGDGE offers two functional groups within one oligomer and given M_w. By matching one PEGDGE oligomer with x times 2 functional PAA groups, the cross-linking ratio x can be calculated. The resulting ratios of PAA:PEGDGE were 1/4, 1/8, and 1/10, which were named in the following as Li_xPAA-PEG$_y$ with $x = 0$, 0.3 and $y = 1/4$, 1/8, 1/10. For the pre-functionalized samples, the respective amount of PEGDGE was added to silicon dispersed in water. The mixture was put in an ultrasonic bath for two cycles of 2 min each and then was dried at 70 °C under vacuum for 1 h. The resulting powder was ground using a pestle and could then be used as the active material. Those samples were named as $Li_{0,0.3}$PAA-PEG$_{1/10@Si}$.

Fabrication of Electrodes Containing PAA-PEG and Partially Neutralized PAA-PEG. Manufacturing of electrodes was done in batches of ca 80 g slurry. By starting with premixing the main solid components—88.5 wt % pestled silicon microparticles (Elkem e-Si 703, d_{50} = 3.59 μm) and 3 wt % carbon black (Imerys, Super C45)—with a helix-type stirrer and an overhead mixer, it was ensured that the conductive carbon black is well distributed around the active material. The premixed powder was then added stepwise to the binder solution (8% binder in the resulting dry electrode) and mixed with a planetary centrifugal mixer (SpeedmixerTM DAC 700.2 VAC-P) in a 150 mL cup. If necessary, some deionized water was added in between to adjust the viscosity and improve mixing efficiency. As a final step, 0.5 wt % single-walled carbon nanotubes (SWCNTs, Tuball) were added to the slurry and mixed thoroughly. After degassing the slurry with the Speedmixer, rheology (rheometer Anton Paar MCR 302) and solid content were measured. If necessary, the solid content was adapted to ∼40 wt %. A check for agglomerates was executed with a Hegman gauge/grindometer before coating. Next, the slurry was cast on a 10 μm copper foil by a doctor blade on a table coater. Based on the solid content, a thickness between 75 and 100 μm was chosen to target the desired loading. The targeted loading was calculated based on the given cathode loading to be matched with the N/P ratio mentioned in the section of full cell assembly. The underlying Si capacity for the calculation was chosen as 1500 mAh g^{-1} to later limit the Si capacity in the full cell via the N/P ratio respectively oversizing of the anode. After casting, the electrodes were dried under vacuum at 80 °C overnight (∼16 h). Afterward, the dried electrodes were calendered once using an Ingecal lab calender with preheating to 80 °C. With that procedure, the anodes were calendered from ca 37 ± 1 μm to ca 33 ± 1 μm in thickness,

Downloaded from pubs.acs.org/aaemcq/article-pdf/9/16/10674/6654359/ae-2026-015488.pdf by KIT BIBLIOTHEK user on 02 November 2026

https://doi.org/10.1021/acsaem.6c01548
ACS Appl. Energy Mater. 2026, 9, 10674−10688

resulting in a coating density increase from ca 0.87 g cm^{-3} to ca 1.00 g cm^{-3}. The final dry electrode thickness was measured using a micrometer gauge (Mitutoyo high accuracy), and the adhesion was analyzed via a 90° peel test (ZwickRoell) with electrode pieces of comparable loading. For this purpose, the electrode stripes (~3 cm broad) were attached with the coating on an adhesive tape, and the copper foil was peeled off. For cohesion measurement, it was done vice versa, namely, copper foil was fixed on the adhesive tape and another adhesive tape on the coating, which was then pulled away to create mechanical failure within the coating layer.

Cell Preparation and Electrochemical Testing

Cell assembly was conducted in an argon-filled glovebox (O_2 < 10 ppm, H_2O < 1 ppm). Both half and full cells were assembled using an electrolyte containing 1.2 M $LiPF_6$/ethylene carbonate (EC), ethyl methyl carbonate (EMC), and dimethyl carbonate (DMC) + 1% vinylene carbonate (VC) + 7% fluoroethylene carbonate (FEC) together with polyethylene-based, ceramic-coated tri-layer separators (21 μm thickness).

Galvanostatic cycling was carried out using a Basytec battery tester, while for cyclic voltammetry (CV) measurements, a Biologic potentiostat was used.

Half-Cell Assembly and Testing. CR2016-type coin cells were assembled using a Si-based anode (Ø = 15 mm), a polyethylene-based, ceramic-coated tri-layer separator (20 μm thick, Ø = 21 mm), 75 μL electrolyte, and lithium metal counter/reference electrode (250 μm thick, Ø = 16 mm). The spacer was used without a spring, and the cell was crimped in the glovebox. The electrode coins were dried at 80 °C under vacuum overnight before half-cell assembly in the glovebox.

The half-cells were cycled between 0.01 and 1.5 V vs Li^+/Li at C-rates of C/20 and C/10 in the first and second cycles, respectively, to allow proper electrode formation. Subsequent cycles were conducted at C/3 with lithiation under constant current constant voltage (CCCV) and delithiation under constant current (CC). In order to use the Si anode only to a limited extent and therefore reduce volume change, the capacity was limited during lithiation of Si to 1500 mAh g^{-1} within the program, which was then also the basis for the C-rate calculation during C-rate tests. CV was measured in the range of 0.01–1.5 V vs Li^+/Li at a scan rate of 0.1 mV s^{-1} at room temperature over four cycles.

Full-Cell Assembly and Testing. Full pouch cells were assembled in a dry room with a dew point below −50 °C. For stacking, a double-sided roll-to-roll coated cathode based on single-crystal NMC811 (94.5% commercial active material, 1% Super C65 carbon black, 1% multi-walled carbon nanotubes (MWCNTs), and 3.5% polyvinylidene fluoride, PVDF) was used in the middle. Two single-sided, lab-coated anodes described above were stacked sandwich-type on both sides of the cathode. With the cathode loading of ~3 mAh cm^{-2} and a size of 4.8 × 4.8 cm^2, the cell capacity was ~150 mAh. The anode (5 × 5 cm^2) loading was calculated based on the capacity limitation of 1500 mAh g_{Si}^{-1} and to match the cathode loading with a negative/positive (N/P) capacity ratio of ~1.01 to 1.17. The cells were dried at 80 °C under vacuum overnight, then filled with 5 mL Ah^{-1} electrolyte and put under vacuum (40 mbar) before sealing them in the glovebox. In preparation for the cycling, each cell was pressed between two acrylic glass plates with two foldback clamps and left to rest for 2 h.

All cells underwent initial formation (2 cycles at C/10, followed by 2 cycles at C/5, and then 3 cycles at C/3) before cycling. Subsequent cycling was done at 1C in the potential range of 3.0–4.2 V vs Li^+/Li, using CCCV in charge and CC in discharge direction, with C/3 check-up cycles every 50th cycle to determine the state of health (SOH) of the cell by comparing the measured C/3 capacity with the initial C/3 capacity. The check-up cycles were also used to include direct internal resistance (DCIR) tests. The cycling of the cells proceeded until SOH = 80%.

Characterization

Fourier-Transform Infrared Spectroscopy (FTIR). FTIR spectra were acquired using a Thermo Scientific Nicolet iS20 spectrometer (Thermo Fisher Scientific, Waltham, USA) with an air-cooled deuterated triglycine sulfate (DTGS) detector in attenuated total reflection (ATR) mode. All spectra were recorded at room temperature in the spectral range of 4000–400 cm^{-1} (resolution of 0.25 cm^{-1}) and baseline corrected using OMNIC (Thermo Fisher Scientific, Waltham, USA).

Differential Scanning Calorimetry (DSC). DSC measurements were done with a Waters Q100 system using aluminum pans under nitrogen and air flow in a temperature range between −60 and 300 °C at a rate of 10 K min^{-1}.

Thermogravimetric Analysis (TGA). TGA was conducted using a Waters Q5000 system with platinum pans and nitrogen/air flow. The measurement was done between 20 and 600 °C with a rate of 20 K min^{-1}.

Scanning Electron Microscopy (SEM)–Energy-Dispersive X-ray Spectroscopy (EDX). SEM images were taken with a TESCAN Mira3 using a 15 keV electron beam and equipped with a ThermoFisher EDX system. A Hitachi IM 4000 Plus with cross-section milling was used for ion polishing.

X-ray Photoelectron Spectroscopy (XPS). A Specs XPS system with monochromatized Al Kα (1486.6 eV) radiation was used for XPS measurements. Survey and detail spectra were recorded with pass energies of 90 and 30 eV at the analyzer, respectively. To compensate for charging effects on the surface, the samples were neutralized with electrons from a flood gun. The C 1s peak of conductive carbon was set to 284.4 eV for binding energy calibration. CasaXPS was used for peak fitting with Shirley-type backgrounds and Gaussian–Lorentzian peak shapes (GL30). For the Si 2p spectra, a peak doublet (Δ = 0.61 eV) was inserted for elemental Si, while a (broader) single peak was adopted for the oxidized Si species (SiO_x and SiO_2). A peak at 532.7 eV was added in the O 1s spectra of pristine samples due to SiO_2. The intensity of this peak was derived from the SiO_2 Si 2p signal, considering the stoichiometry and the atomic sensitivity factors of Si 2p and O 1s peaks.

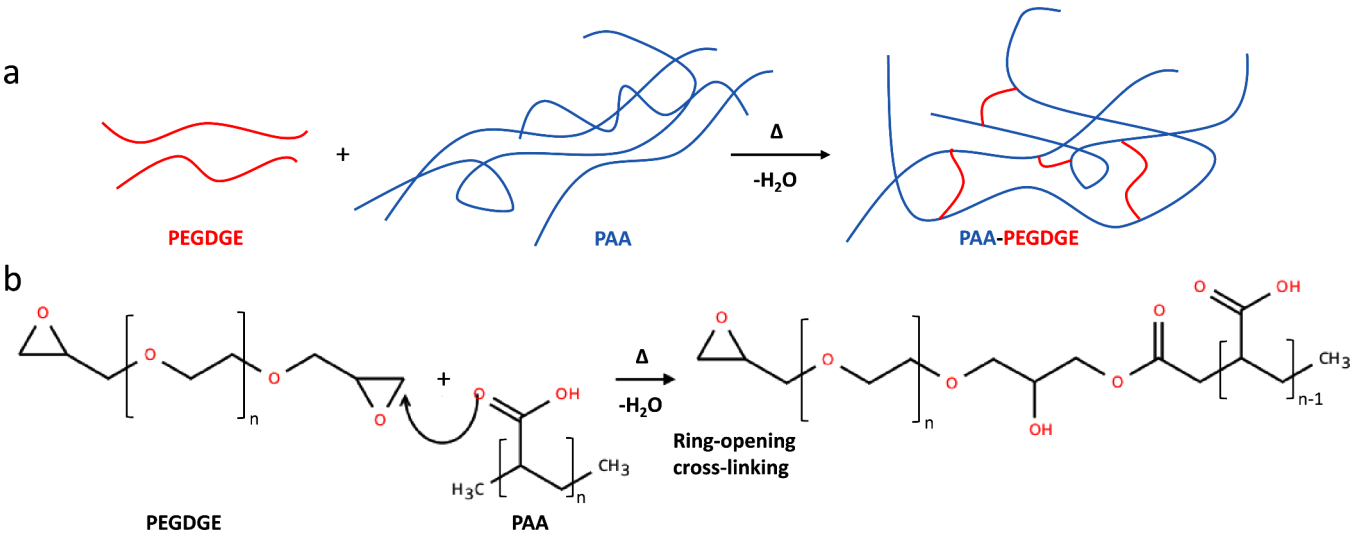
■ RESULTS AND DISCUSSION

Since the pronounced volume changes of Si anodes lead to poor electrode integrity and limited cycling stability, the objective of this work was to design a binder specifically optimized to address this challenge. Cross-linkers are known to enhance binder performance by reinforcing the polymer network and thereby improving its mechanical resilience. Based on that, we pursued a strategy in which a flexible segment was introduced between rather rigid binder strands. To achieve this, a straightforward approach—in situ cross-linking—was used to incorporate a suitable cross-linker into the binder.[28] The bifunctional oligomer PEGDGE was selected for its ability to enable in situ cross-linking with the PAA binder in aqueous media via an epoxide ring-opening reaction, which is shown in Scheme 1. Additionally, the beneficial properties of PEGDGE with regard to ionic conductivity, flexibility, dispersion of slurries, and cohesion[22,51] have already been proven in various applications, such as polymer electrolytes.[50] The same properties are highly desirable for Si anodes since they can contribute to enhanced ion conductivity and flexibility of the binder structure and a better accommodation of the volume changes upon lithiation/delithiation, leading overall to improved performance. In order to prove the in situ cross-linking concept, pre-studies with both dissolved PAA binder and PEGDGE were conducted. It is known that ions from the copper foil can influence the binder cross-linking and adhesion of PAA on the copper substrate via copper carboxylates.[34] Therefore, a mixture of PAA and PEGDGE was put on both copper foil and a polymeric foil as a reference and left in the oven under vacuum for drying.

Downloaded from pubs.acs.org/aaemcq/article-pdf/9/16/10674/6654359/ae-2026-015488.pdf by KIT BIBLIOTHEK user on 02 November 2026

https://doi.org/10.1021/acsaem.6c01548
ACS Appl. Energy Mater. 2026, 9, 10674−10688

Scheme 1. (a) Broad Scheme Highlighting the Networking by Cross-Linking of PAA and PEGDGE; (b) Proposed Epoxide Ring-Opening Cross-linking Reaction between PAA and the Cross-linker PEGDGE



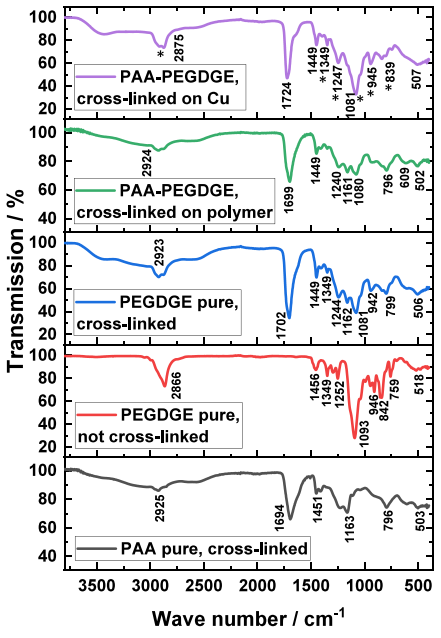


Figure 1. FTIR results of the PAA-PEGDGE mixture with successful cross-linking on copper foil (violet) or unsuccessful cross-linking on the polymer foil substrate (green). For comparison, results of pure PAA (black), pure PEGDGE (red), and pure cross-linked PEGDGE (blue) were added. The cross-linking on the copper foil substrate is indicated by the C–O–C stretching vibrations of the PEG segments at 1081 and 944 cm^{-1}, significantly increased C–H stretching vibrations of methylene in PEG at 2875 and 2910 cm^{-1}, new absorption bands at 1349 and 839 cm^{-1}, and C–C stretching vibration at 1247 cm^{-1}, all marked in the figure with a *.

FTIR analysis of the dried films (see Figure 1) demonstrates that the substrate plays a significant role in polymerization and cross-linking reactions. Notably, the C–O–C stretching vibrations of the PEG segments at 1081 and 944 cm^{-1} are observed for the film on copper foil but not for the polymeric foil. Additionally, the C–H stretching vibrations of methylene in PEG at 2875 and 2910 cm^{-1} significantly increased compared to the sample cross-linked on polymer foil. Also, new absorption bands at 1349 and 839 cm^{-1}, as well as the C–C stretching vibration at 1247 cm^{-1} are observed in the copper-supported film.[52] All other peaks are the same as in either pure PAA or pure PEGDGE. Therefore, the listed changes indicate cross-linking of PAA and PEGDGE only on copper foil.

The successful cross-linking of PAA and PEGDGE on copper foil was also confirmed by XPS measurements. The survey spectra are shown in Figure S1 with spectra of (a) Si powder with Si 2p and 2s peaks, along with C 1s and O 1s peaks; (b) PAA with C 1s and O 1s peaks; and (c) cross-linked PAA-PEG with C 1s and O 1s peaks as well. Both polymer samples were dried on copper foil before the measurements. The corresponding detail spectra are shown in Figure S2. As expected, the Si powder exhibited a SiO_x/SiO_2 layer on the Si^0 substrate together with organic residues likely originating from the processing. The PAA on copper shows respective peaks corresponding to the polymer backbone and carboxylic acid groups, along with some cross-linked part with C–O ether groups. In contrast, the C 1s spectrum of the PAA-PEG sample on copper shows a pronounced increase of the C–O peak intensity due to the ether groups of PEG and additional cross-linking.

In order to analyze the thermal properties of the polymers, thermogravimetric analysis (TGA) and differential scanning calorimetry (DSC) were conducted. TGA results are shown in Figure S3a–d. For pure PAA powder (Figure S3a), an initial weight loss can be observed already in the lower temperature range (from 50 to 100 °C), which is attributed to the removal of water from the sample. In contrast, the cross-linked PAA shows the onset of water loss at a slightly higher temperature (~80 °C), which may be related to further cross-linking generating water. Both seem to be thermally stable until >200 °C. A similar observation can be made for pure PEGDGE (Figure S3c). Therefore, both polymers match well from a thermal-stability perspective. The main difference becomes obvious in the derived mass, that is, mass loss per °C. For cross-linked PAA (Figure S3b), the loss occurs stepwise at 150–200 °C, which could be due to a minor decarboxylation reaction, then

Downloaded from pubs.acs.org/aaemcq/article-pdf/9/16/10674/6654359/ae-2026-015488.pdf by KIT BIBLIOTHEK user on 02 November 2026

https://doi.org/10.1021/acsaem.6c01548
ACS Appl. Energy Mater. 2026, 9, 10674−10688

225–300 °C with anhydride formation, and finally 300–350 and 350–480 °C from thermal degradation of the corresponding polyacrylic anhydride[53] with ∼7% remaining residual mass at 600 °C. PEGDGE (Figure S3c) only shows one big peak from 200 to 425 °C with almost no residual mass left above this temperature. The decomposition then occurs for both C–O and C–C bonds.[54] Finally, the combination of both—the cross-linked PAA-PEGDGE—shows characteristics from both PAA and PEGDGE (Figure S3d). The initial weight loss at around 100 °C is attributed to remaining cross-linking releasing water, along with desorption of moisture still trapped in the polymer after drying. A smaller peak at ∼300 °C seems to be the same decomposition process observed as a shoulder in the pure PEGDGE diagram. At 400 °C the decomposition of PAA anhydride occurs, followed by a sharp peak at around 425 °C showing the decomposition of PEGDGE C–O and C–C bonds. As for pure cross-linked PAA, a residue of ∼7% remains at 600 °C.

The DSC results are shown in Figure S3e,f. The pure cross-linked PAA (Figure S3e) shows a small peak at 59.7 °C and a glass transition at T_g 158.7 °C. At T_c 220 °C, a strong crystallization peak occurs. For pure PEGDGE, the used temperature range cannot properly show its low T_g, which lies between –60 and –45 °C.[49,50,55,56] The cross-linked PAA-PEGDGE (Figure S3f) shows a T_g at ca –5 °C (compared to 102–126 °C for pure PAA[57,58]). Lowering of the T_g of the PAA in the composite polymer due to the PEG segments results in increased flexibility and mobility (less crystallinity of the polymer) and therefore higher ionic conductivity.[45] The DSC of PAA-PEGDGE also shows a broad crystallization peak at T_c 105 °C together with an endothermic melting peak at T_m 160 °C.

After investigation of the different polymers (without Si), both TGA and DSC analyses were also carried out on anodes containing pure PAA and cross-linked PAA-PEGDGE. In TGA (Figure S4a–d), up to 250 °C, all samples only show water loss, and a different behavior of the samples can only be observed at temperatures beyond. The pure Li_0PAA anode (Figure S4a) shows only a strong peak at 280 °C and then again faster mass loss at 450 °C. For the Li_0PAA-PEG$_{1/10}$ anode (Figure S4b), the same peak at 280 °C is observed, but with a shoulder at 320 °C. The faster mass loss at higher temperatures starts at ∼475 °C. In the case of $Li_{0.3}$PAA-PEG$_{1/10}$ (Figure S4c), the strong peak is shifted to 300 °C and accompanied by another peak at 340 °C, which has a shoulder at 390 °C. In the case of the functionalized sample $Li_{0.3}$PAA-PEG$_{1/10@Si}$ (Figure S4d), the peak at 280 °C and a second peak at 330 °C with a shoulder at 350 °C are followed by a rather constant mass loss. This sample also shows the highest residual mass of all samples at the end of the ramp at 600 °C. Generally, the samples containing PEG have slightly higher residual mass at 600 °C than the pure PAA anodes, which could be an indication of higher thermal stability. In DSC (Figure S4e–h), only minor differences can be observed. In all cases, there are two small exothermic peaks at 75 and 240 °C; only for Li_0PAA (Figure S4e), the second peak is slightly shifted to 225 °C. Furthermore, Li_0PAA and Li_0PAA-PEG$_{1/10}$ have roughly the same peak intensities for both peaks (Figure S4e,f). In contrast, for the partially neutralized samples $Li_{0.3}$-PEG$_{1/10}$ and $Li_{0.3}$-PEG$_{1/10@Si}$ (Figure S4g,h), the second peak at a higher temperature has much lower intensity than the one at 75 °C, showing the impact of the neutralization on the polymer properties.

Important parameters determining the quality of electrodes are adhesion of the electrode layer to the substrate and cohesion within the layer, especially to quantify the impact of a binder on the mechanical behavior. As shown in Figure 2, Li_0PAA exhibits much higher adhesion compared to Li_0PAA-PEG$_{1/10}$; however, the cohesion improves for the latter. Both samples show lower performance in this regard compared to the partially neutralized samples. For the partially neutralized PAA, the incorporation of PEG ($Li_{0.3}$PAA-PEG$_{1/10}$) significantly increases adhesion in comparison to $Li_{0.3}$PAA. This is likely due to stronger interaction between the binder and the Cu substrate at this pH, with its naturally passivated surface with species including Cu^{2+} ions. Due to the ion-transport ability of PEG, the interaction with Cu cations could be enhanced, explaining stronger adhesion of the $Li_{0.3}$PAA-PEG$_{1/10}$ binder.[34] However, the cohesion is reduced to approximately half of that of $Li_{0.3}$PAA, which can be attributed to smaller interactions between carboxylic acid groups and the Si particle surface, since the groups get partially occupied by crosslinks to the soft and flexible PEG. With Si functionalization ($Li_{0.3}$PAA-PEG$_{1/10@Si}$), the interaction between the Si surface and binder gets focused on the comparably short-chained PEG, which allows a more organized interaction with the Si surface and PAA, resulting in a kind of bridging. This can be the reason for a further increase in cohesion, while the adhesion is comparable to $Li_{0.3}$PAA-PEG$_{1/10}$. Therefore, it can be concluded that both $Li_{0.3}$PAA-PEG$_{1/10}$ and $Li_{0.3}$PAA-PEG$_{1/10@Si}$ show improved mechanical stability by the addition of PEG, as reflected by their high adhesion values, which should significantly mitigate delamination. Even though cohesion is lower than that of $Li_{0.3}$PAA, it is still sufficient to ensure interparticle stability. This balance between high adhesion and adequate cohesion is critical for maintaining electrode integrity, particularly in applications where mechanical stress due to repeated lithiation/delithiation could otherwise compromise performance.

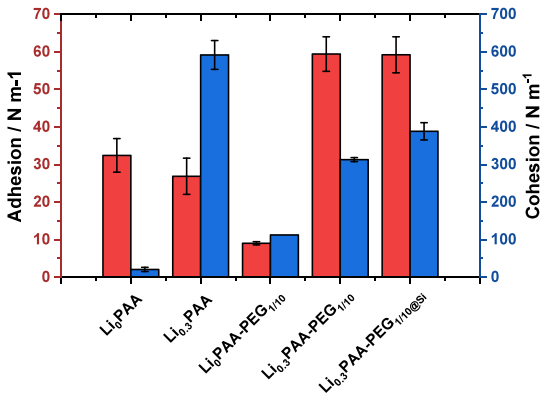


Figure 2. Adhesion (red bars) and cohesion (blue bars) of electrodes containing Li_0PAA, $Li_{0.3}$PAA, Li_0PAA-PEG$_{1/10}$, $Li_{0.3}$PAA-PEG$_{1/10}$, and $Li_{0.3}$PAA-PEG$_{1/10@Si}$.

To gain further understanding of the impact of the PEG cross-linker on the anode and to be able to interpret the later-shown post-mortem results, SEM images were taken of the pristine anodes. The top-view and cross-section images of the samples Li_0PAA-PEG$_{1/10}$, $Li_{0.3}$PAA-PEG$_{1/8}$, $Li_{0.3}$PAA-PEG$_{1/10}$, and $Li_{0.3}$PAA-PEG$_{1/10@Si}$ are shown in Figure S5. Without partial neutralization of PAA or with a higher amount of PEG, the distribution of conductive additive in the anodes is rather inhomogeneous. This seems to be much improved for $Li_{0.3}$PAA-PEG$_{1/10}$ and especially the functionalized sample

Downloaded from pubs.acs.org/aaemcq/article-pdf/9/16/10674/6654359/ae-2026-015488.pdf by KIT BIBLIOTHEK user on 02 November 2026

https://doi.org/10.1021/acsaem.6c01548
ACS Appl. Energy Mater. 2026, 9, 10674–10688

$Li_{0.3}$PAA-$PEG_{1/10@Si}$. To further probe the pristine electrode surfaces and assess possible chemical variations introduced by different binder modifications, XPS measurements were carried out. The survey spectra of anodes with Li_0PAA-$PEG_{1/10}$, $Li_{0.3}$PAA-$PEG_{1/10}$, and $Li_{0.3}$PAA-$PEG_{1/10@Si}$ are shown in Figure S6. As expected, all samples show Si 2p and 2s peaks of the active material and C 1s and O 1s peaks of the binder and conductive additives.

Figure 3 shows the detail spectra in the Si 2p, C 1s, and O 1s regions for Li_0PAA, Li_0PAA-$PEG_{1/10}$, $Li_{0.3}$PAA, $Li_{0.3}$PAA-$PEG_{1/10}$, and $Li_{0.3}$PAA-$PEG_{1/10@Si}$. The Si 2p peaks are comparable for all three samples and similar to the pattern of pure Si powder (see above). In the C 1s region, four peaks due to sp^2-C (C=C), sp^3-C (C–C/C–H), C–O, and O–C=O species can be observed with increasing binding energy for all samples. Similarly, three features due to C–O, SiO_2, and C=O species are observed in the O 1s spectra.[59] When comparing the spectra of Li_0PAA-$PEG_{1/10}$ and Li_0PAA (see also our previous work[38]), the impact of PEG is visible. The intensity of the C–O peak is compared to both sp^2-C and sp^3-C and is much higher for Li_0PAA-$PEG_{1/10}$ than for Li_0PAA, and this increase of C–O can also be seen in the O 1s spectra. The increased C–O contribution is consistent with the formation of C–O–C cross-linking between PAA and PEG in Li_0PAA-$PEG_{1/10}$, although a contribution from PEG itself cannot be excluded. In the case of $Li_{0.3}$PAA- $PEG_{1/10}$, the intensity of the C 1s C–O peak is even higher, especially when compared to the sp^3-C peak. As the amount of added PEGDGE to the anode is exactly the same as for Li_0PAA-$PEG_{1/10}$, this observation can indicate a higher cross-linking ratio between PAA and PEGDGE for the neutralized sample. This trend is even more pronounced for the functionalized sample $Li_{0.3}$PAA-$PEG_{1/10@Si}$. It can be

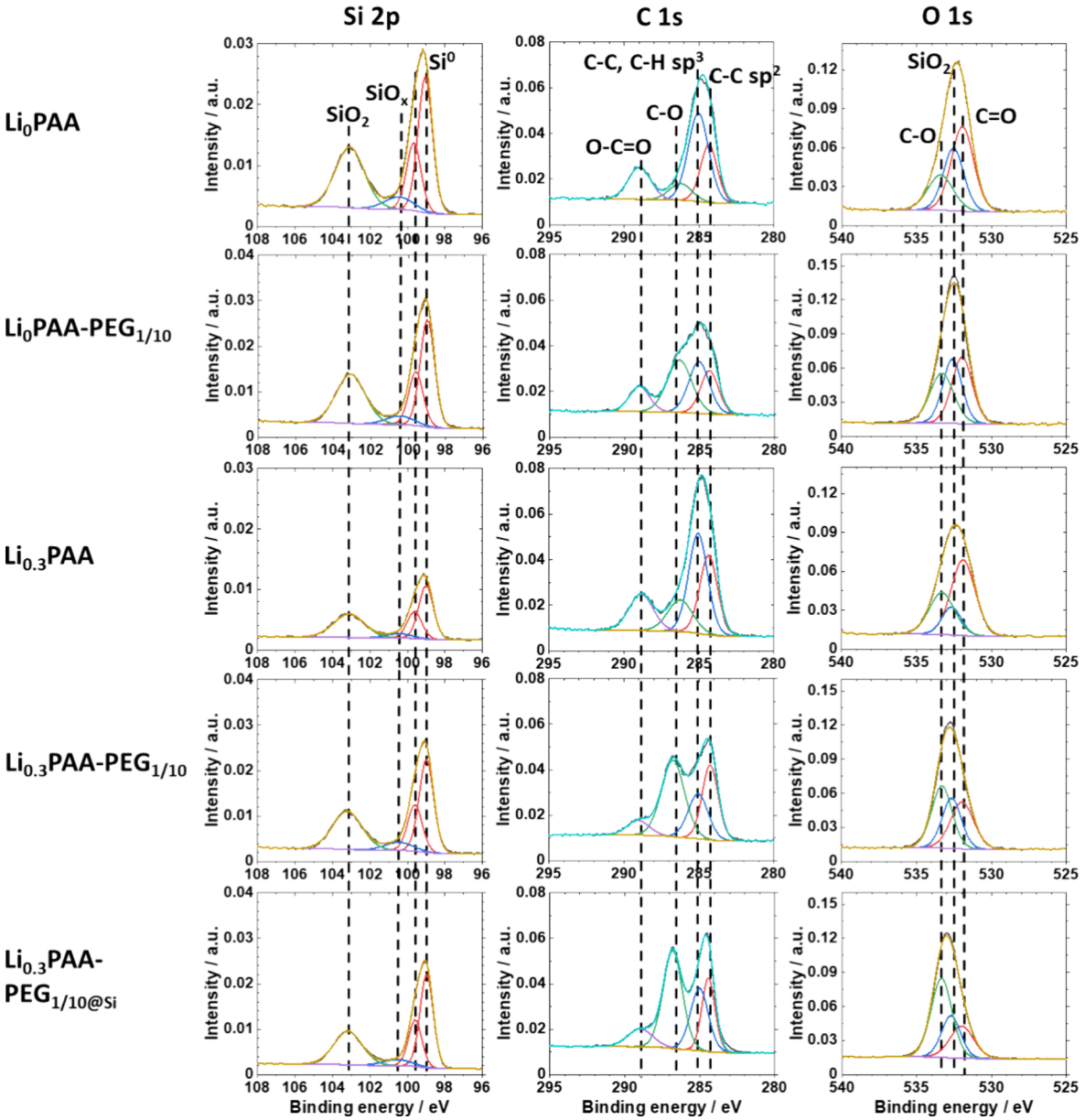


Figure 3. XPS detail measurements in the Si 2p, C 1s, and O 1s regions from pristine electrodes containing Li_0PAA, Li_0PAA-$PEG_{1/10}$, $Li_{0.3}$PAA, $Li_{0.3}$PAA-$PEG_{1/10}$, and $Li_{0.3}$PAA-$PEG_{1/10@Si}$.

https://doi.org/10.1021/acsaem.6c01548
ACS Appl. Energy Mater. 2026, 9, 10674–10688

Downloaded from pubs.acs.org/aaemcq/article-pdf/9/16/10674/6654359/ae-2026-015488.pdf by KIT BIBLIOTHEK user on 02 November 2026

explained by the PAA polymer conformation, which is coiled in acidic form and rather stretched and detangled in the neutralized form.[60] Therefore, the acidic form tends to form intramolecular interactions, causing steric hindrance for the PEGDGE oligomer to interact with the carboxylic acid groups. For the rather decoiled conformation of $Li_{0.3}$PAA, PEGDGE has a better chance to cross-link with the carboxylic acid groups. The even higher C–O contribution for the functionalized $Li_{0.3}$PAA-$PEG_{1/10@Si}$ sample indicates that the Si functionalization with PEGDGE enables an even stronger interaction with $Li_{0.3}$PAA, and therefore a higher cross-linking ratio. It is necessary to point out potential physical adsorption of PEGDGE on the Si surface besides cross-linking. Nevertheless, a comparable study with another implementation scenario of PEG[47] shows the covalent bonding of PEGDGE, which could help to increase the number of PAA chains bonding with the Si surface by a more ordered steric situation. This would then lead to higher stability and therefore cohesion, as already shown in Figure 2.

In order to get a first impression on the impact of PEGDGE on the electrochemical properties of the electrodes, CV measurements were conducted, as displayed in Figure 4. Two cathodic peaks and two anodic peaks can be observed for all samples. The first cycle (black) is different, as the microcrystalline Si (or part of it, when capacity is limited) first has to form amorphous Li_xSi phases during alloying. For the ongoing cycling, the first cathodic peak at 0.18–0.20 V vs Li^+/Li is assigned to the lithiation of amorphous Si to P-I phase (LiSi) together with the phase transition from P-I to P-II (Li_7Si_3). The second cathodic peak at 0.01 V vs Li^+/Li is related to the P-III formation, that is, lithiation of Si in metastable Li-Si amorphous phases to $Li_{3.16}$Si and then probably crystalline Si (<50 mV vs Li^+/Li). The anodic peaks show delithiation of the Si–Li alloys in a two-step lithium extraction process to amorphous Si. First, (partial) decomposition of the highly lithiated phase P-III with $Li_{3.16}$Si takes place toward P-II at 0.4 V vs Li^+/Li (for Li_0PAA at 0.36 V vs Li^+/Li); then further removal of Li toward P-I happens at 0.53 V vs Li^+/Li.[61−64] For the samples Li_0PAA-PEG and $Li_{0.3}$PAA-PEG, where PEGDGE is added to the binder, the first cathodic and the second anodic peaks are slightly shifted to 0.2 V vs Li^+/Li and 0.515 V vs Li^+/

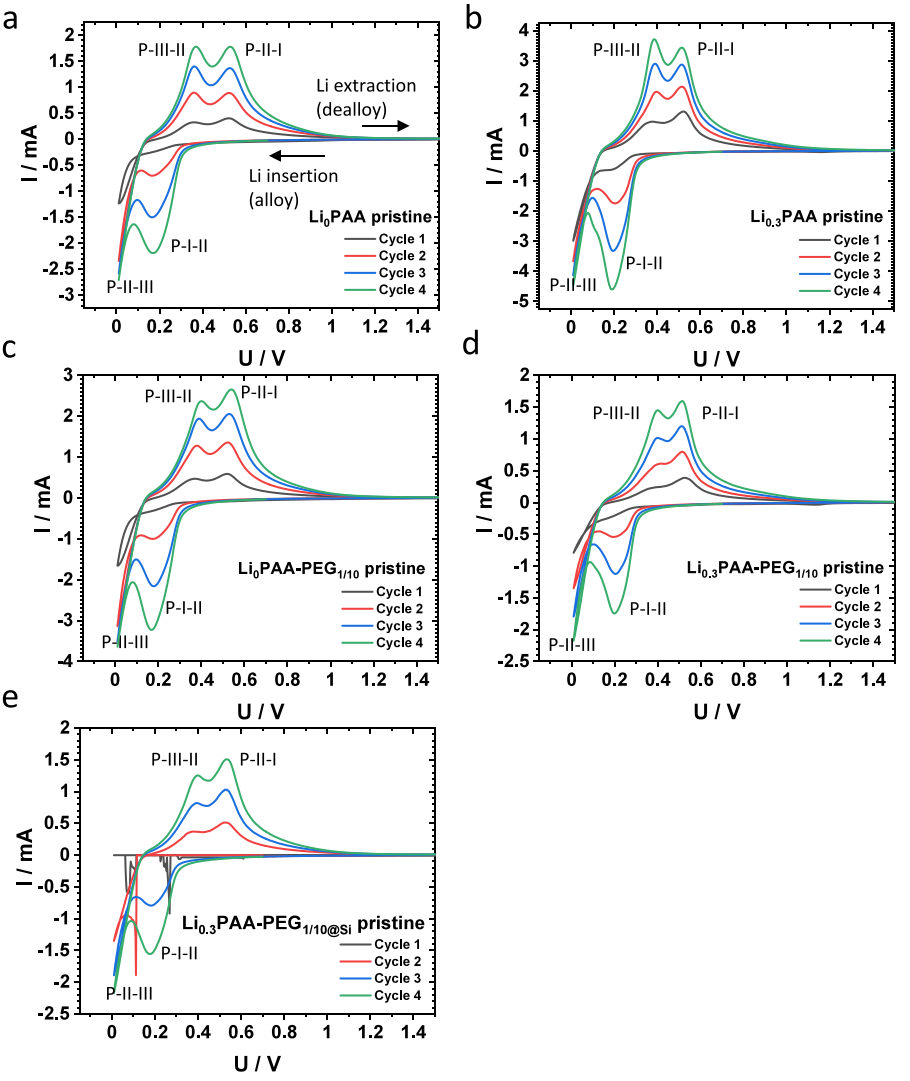


Figure 4. Cyclic voltammograms of the first four cycles of pristine anodes containing (a) Li_0PAA, (b) $Li_{0.3}$PAA, (c) Li_0PAA-$PEG_{1/10}$, (d) $Li_{0.3}$PAA-$PEG_{1/10}$, and (e) $Li_{0.3}$PAA-$PEG_{1/10@Si}$ in the voltage range 0.01–1.5 V vs Li^+/Li with a scan rate of 0.1 mV s^{-1}. The cell in (e) had a contact issue during the first cycle but cycled correctly in the subsequent cycles.

Downloaded from pubs.acs.org/aaemcq/article-pdf/9/16/10674/6654359/ae-2026-015488.pdf by KIT BIBLIOTHEK user on 02 November 2026

https://doi.org/10.1021/acsaem.6c01548
ACS Appl. Energy Mater. 2026, 9, 10674−10688

Li, respectively. Therefore, these peaks come closer together, which can indicate higher reversibility induced by PEGDGE. For all samples, increasing peak intensities are observed with increasing cycle number, meaning higher Li^+ concentration and therefore facilitated Li^+ diffusion paths allowing storage of more Li^+. None of the samples show irreversible peaks, which verifies that all of them are electrochemically stable. It can already be seen by comparison of the results from Li_0PAA and $Li_{0.3}$PAA that the partial neutralization of PAA makes a difference in the Li insertion as well as extraction direction. Especially, the cathodic peak at ~0.2 V vs Li^+/Li is different, and the superimposed transition peaks are visible as shoulders of the main peak for $Li_{0.3}$PAA. In addition, the intensity increases significantly; hence, the diffusion and storage of lithium ions into the silicon are significantly larger. This can be caused by the presence of Li^+ ions in the binder and also by better contact and transport of ions due to decoiled PAA polymer conformation.[34,60] In the dealloying direction, the peak intensities are also higher for $Li_{0.3}$PAA, and the ratio is not equal to that for Li_0PAA, but the peak of transition P-III–II is higher than that of P-II–I. Generally, these observed differences indicate better electrode integrity of partially neutralized PAA and more homogeneous alloying of Si as the anodes are oversized; therefore, all parts get only partially lithiated. In case of acidic PAA, the anodes seem not as mechanically stable; thus, detaching particles will not be included in alloying anymore, while other parts then will be lithiated more. This inhomogeneity will then lead to a shift of higher lithiated phases and generally less intensity. In the case of Li_0PAA-$PEG_{1/10}$, the cathodic P-I–II peak and anodic P-II–I peak are more pronounced than in Li_0PAA with generally higher intensities, which could indicate better Li^+ transport/storage due to PEG addition and its ion transport ability. $Li_{0.3}$PAA-$PEG_{1/10}$ and $Li_{0.3}$PAA-$PEG_{1/10@Si}$ show the same peak ratios as the non-neutralized sample, but with the cathodic peak including shoulders of a superimposed transition like $Li_{0.3}$PAA. Interestingly, compared to the latter, the intensities of both samples are slightly smaller, which shows lower ion concentration and therefore less beneficial diffusion paths because of the cross-linkage.

Next, galvanostatic cycling tests were carried out to further examine the electrochemical performance of the anodes in both half-cell and full-cell configurations. The half-cell results, with limited capacity to 1500 mAh g^{-1}_{Si}, are shown in Figure 5, split into anodes based on Li_0PAA (Figure 5a) and $Li_{0.3}$PAA (Figure 5b). The respective coulombic efficiencies (CEs) are shown in Figure 5c,d. For the anodes based on Li_0PAA (Figure 5a), the standard Li_0PAA anode obviously shows the most stable cycling behavior, while the incorporation of PEG gradually deteriorates capacity retention. Among these, Li_0PAA-$PEG_{1/10}$ maintains relatively stable cycling up to approximately 20 cycles, after which capacity fading becomes evident. Interestingly, when PEG is grafted directly onto the Si surface (Li_0PAA-$PEG_{1/10@Si}$), cycling performance further declines. One reason could be that the high amount of PEG at the active material surface induces less favorable side reactions during cycling. These observations are also supported by the CE (Figure 5c) with a slightly lower CE of Li_0PAA-$PEG_{1/10}$ during cycling compared with that of Li_0PAA.

The partially neutralized $Li_{0.3}$PAA (Figure 5b) shows a somewhat different trend. Even though $Li_{0.3}$PAA again offers highly stable cycling, $Li_{0.3}$PAA-$PEG_{1/10}$ maintains the same stability for ~40 cycles—about twice as long as the non-neutralized counterpart—highlighting the beneficial effect of partial lithium neutralization on binder elasticity and ionic conductivity. Again, both the first cycle efficiency (FCE) and CE (Figure 5d) of $Li_{0.3}$PAA-$PEG_{1/10}$ are, however, slightly lower than those of $Li_{0.3}$PAA. The $Li_{0.3}$PAA-$PEG_{1/10@Si}$ electrode, despite its less stable capacity retention beyond 20 cycles, shows an improved FCE of 93.5%, exceeding that of $Li_{0.3}$PAA (92.2%). This suggests that the covalent anchoring of PEG on the Si surface may initially mitigate irreversible Li consumption by stabilizing the interfacial chemistry, although long-term cycling stability remains limited—likely due to progressive detachment or fracture of active particles.

The rate capability measurements (Figure 5e) show favorable performance for both $Li_{0.3}$PAA and $Li_{0.3}$PAA-$PEG_{1/10}$, with slightly better capacity retention of $Li_{0.3}$PAA-$PEG_{1/10}$ at high C-rates, possibly owing to enhanced Li^+ transport through the flexible cross-linked network. In contrast, $Li_{0.3}$PAA-$PEG_{1/10@Si}$ suffers from significant capacity fading at C-rates higher than 1.5 C, and it does not recover its initial capacity at C/3 after the C-rate test.

To assess the binder modification effects in a more practical system, the optimized anodes were further tested in full pouch cells against NMC811 cathodes. The cells were cycled at 1C, with C/3 check-up cycles every 50th cycle until the state of health (SOH) reached 80%. Each sample was tested with 3 cells to ensure reproducibility (Figure 6). The performance of the Li_0PAA-based anodes is shown in Figure 6a and that of the $Li_{0.3}$PAA-based anodes is shown in Figure 6c. The corresponding CEs of the formation process for the Li_0PAA-based anodes and the $Li_{0.3}$PAA-based anodes are shown in Figure 6b,d, respectively. Similar to the findings in half-cell tests, the Li_0PAA electrode shows better capacity retention than Li_0PAA-$PEG_{1/10}$ and very comparable CEs in the formation cycles, whereas increasing the PEG amount leads to severe capacity fading and poor cycling performance. A possible reason could be that an excessive amount of PEG weakens the cohesion of the anode and could partly bind Li^+ ions.

In the case of $Li_{0.3}$PAA-based anodes (Figure 6d), the FCEs in formation are very comparable; $Li_{0.3}$PAA-$PEG_{1/10@Si}$ offers slightly higher FCE, but within measurement tolerances. The cycling results in Figure 6c again reveal decreasing performance with a higher PEG ratio, but interestingly, the $Li_{0.3}$PAA-$PEG_{1/10}$ sample does not show cycling performance comparable to $Li_{0.3}$PAA, as expected from the results of half-cell cycling. In contrast, $Li_{0.3}$PAA-$PEG_{1/10@Si}$ achieved comparable capacity retention based on C/3 check-up cycles with a slightly weaker 1C performance in between but with rather linear degradation instead of an increasing fading rate with a higher cycle number. This indicates a different fading mechanism, which is investigated next with post-mortem studies.

After cycling to SOH = 80%, the cells were disassembled, and the anodes were subjected to post-mortem analysis. Post-mortem CV was performed to evaluate residual electrochemical activity and possible degradation mechanisms (Figure S7). All samples show a difference in the first cycle compared to the subsequent cycles. These changes can be explained by the fact that the post-mortem electrodes were drawn from a rather Li^+-depleted system and put in a half cell with fresh Li and electrolyte. Therefore, the post-mortem anodes are, compared to the aged full cell system, in a relatively high lithiation state, and a certain passivation occurs. The Li_0PAA-based electrodes (Figure S7a), Li_0PAA-$PEG_{1/10}$ (Figure S7c) and

Downloaded from pubs.acs.org/aaemcq/article-pdf/9/16/10674/6654359/ae-2026-015488.pdf by KIT BIBLIOTHEK user on 02 November 2026

https://doi.org/10.1021/acsaem.6c01548
ACS Appl. Energy Mater. 2026, 9, 10674−10688

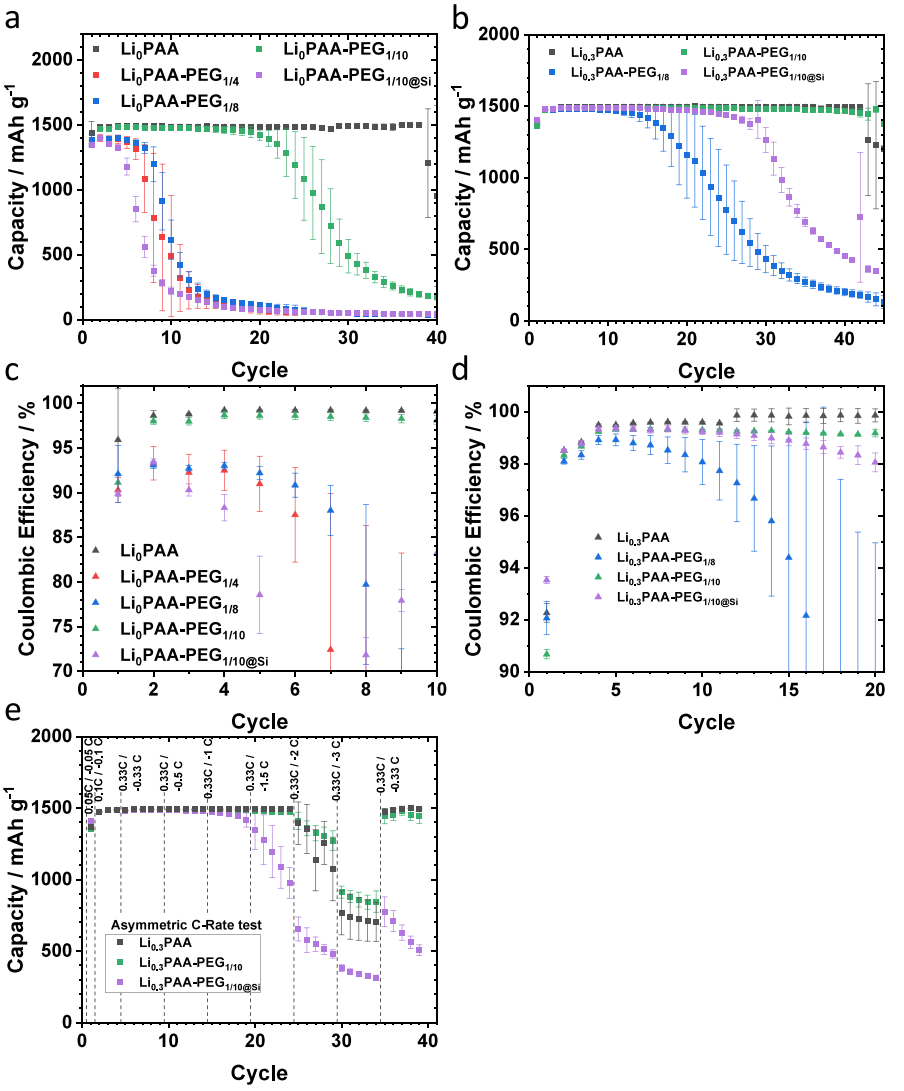


Figure 5. Half-cell C/3 cycling performance of anodes based on (a) Li_0PAA and respective modifications and (b) $Li_{0.3}$PAA and respective modifications. (c) and (d) corresponding Coulombic efficiencies. (e) Half-cell C-rate test with anodes based on $Li_{0.3}$PAA, $Li_{0.3}$PAA-PEG$_{1/10}$, and $Li_{0.3}$PAA-PEG$_{1/10@Si}$ with constant lithiation at C/3 and varied delithiation C-rates up to 3C. All of the above tests were conducted with a minimum of three cells each.

Li_0PAA-PEG$_{1/10@Si}$ (Figure S7e) still show the same type of peaks in the cathodic and anodic directions; and no drastic changes can be found when comparing with the pristine samples (Figure 4), indicating that the fundamental Si alloying/dealloying mechanism remains largely preserved after extended cycling. Only the second anodic peak shifted to a slightly lower voltage (from 0.53 to 0.5 V vs Li^+/Li) for the samples with Li_0PAA and Li_0PAA-PEG$_{1/10@Si}$, suggesting improved reversibility and reduced polarization. In contrast, the voltage increased from 0.515 to 0.53 V vs Li^+/Li for Li_0PAA-PEG$_{1/10}$, indicative of increased overpotential and kinetic hindrance after prolonged cycling. Furthermore, the peak intensities of the latter sample increased significantly compared to the sample without PEGDGE, which can indicate facilitated Li^+ transport. In the case of $Li_{0.3}$PAA-based samples, the post-mortem CVs show notably different features. Both $Li_{0.3}$PAA and $Li_{0.3}$PAA-PEG$_{1/10}$ show merged cathodic peaks and one anodic peak, implying structural and interfacial degradation that disrupts the typical multi-step alloying/dealloying behavior of Si. In contrast, $Li_{0.3}$PAA-PEG$_{1/10@Si}$ shows a comparable pattern to the Li_0PAA-containing anodes, preserving the cathodic and anodic double peaks. This could mean that the alloying mechanism is still maintained for these samples at SOH = 80%, while $Li_{0.3}$PAA and $Li_{0.3}$PAA-PEG$_{1/10}$ degraded differently at the same SOH after 150 cycles. This observation emphasizes that the covalent anchoring of PEG to the Si surface may mitigate mechanical degradation, preserving reversible Si lithiation pathways during extended cycling.

Regarding mechanical degradation, post-mortem SEM images were taken for the anodes with Li_0PAA, Li_0PAA-PEG$_{1/10}$, $Li_{0.3}$PAA, $Li_{0.3}$PAA-PEG$_{1/8}$, $Li_{0.3}$PAA-PEG$_{1/10}$, and $Li_{0.3}$PAA-PEG$_{1/10@Si}$ to elucidate the damage induced by the volume changes upon cycling (see Figure 7). Surface morphologies are shown in the left and middle-left, while the cross-sections are depicted in the middle-right and right.

Among the binder systems, the Li_0PAA-PEG$_{1/10}$ seems to have fewer cracks than the other samples (also compared to Li_0PAA), suggesting that the incorporation of PEGDGE helps

Downloaded from pubs.acs.org/aaemcq/article-pdf/9/16/10674/6654359/ae-2026-015488.pdf by KIT BIBLIOTHEK user on 02 November 2026

https://doi.org/10.1021/acsaem.6c01548
ACS Appl. Energy Mater. 2026, 9, 10674−10688

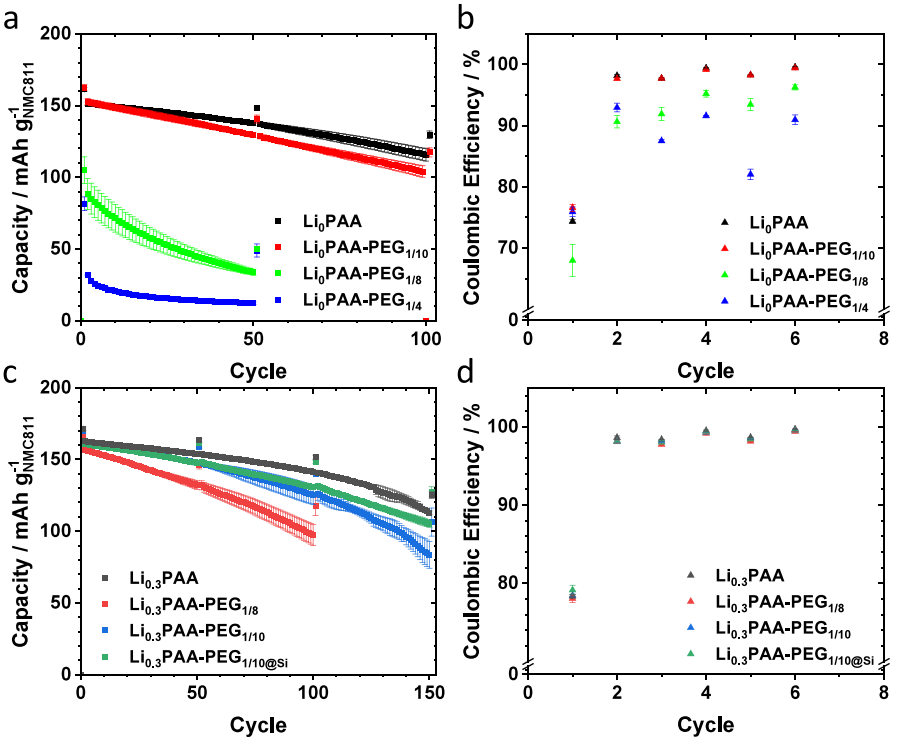


Figure 6. Full cell cycling performance of anodes based on (a) Li_0PAA and its respective modifications and (c) $Li_{0.3}PAA$ and its respective modifications, cycled against NMC811 at 1C with C/3 check-up cycles every 50th cycle. (b) and (d) corresponding Coulombic efficiencies. All the above tests were conducted with a minimum of two cells each.

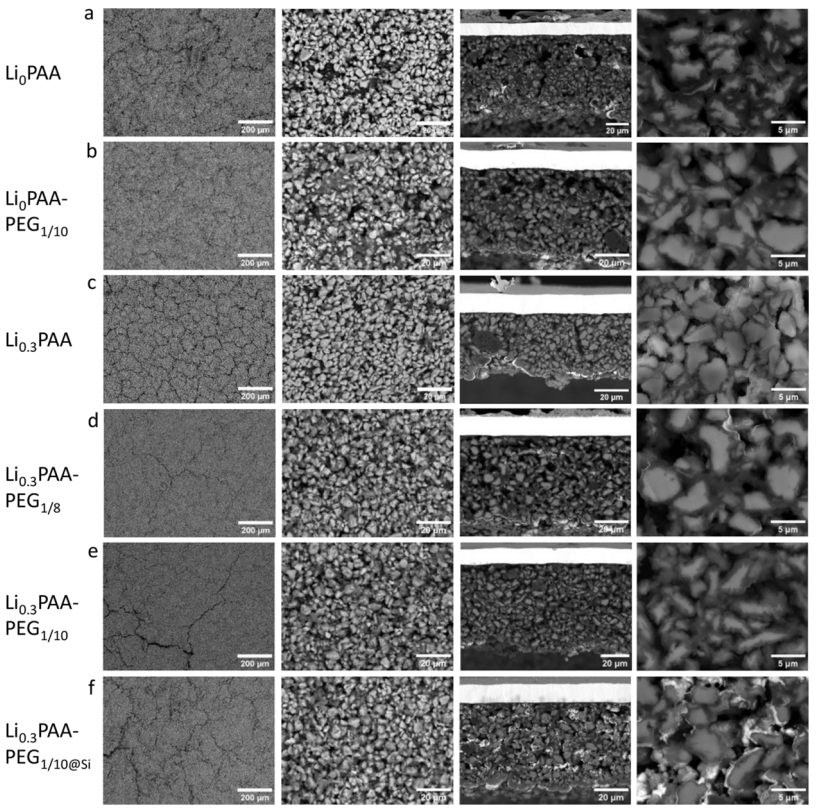


Figure 7. SEM images from a top-view perspective (left and middle -left) and cross-section (middle-right and right) with different magnifications of post-mortem electrodes containing (a) Li_0PAA, (b) Li_0PAA-$PEG_{1/10}$, (c) $Li_{0.3}PAA$, (d) $Li_{0.3}PAA$-$PEG_{1/8}$, (e) $Li_{0.3}PAA$-$PEG_{1/10}$, and (f) $Li_{0.3}PAA$-$PEG_{1/10@Si}$ after 1C cycling until SOH = 70–80%.

Downloaded from pubs.acs.org/aaemcq/article-pdf/9/16/10674/6654359/ae-2026-015488.pdf by KIT BIBLIOTHEK user on 02 November 2026

https://doi.org/10.1021/acsaem.6c01548
ACS Appl. Energy Mater. 2026, 9, 10674−10688

to maintain the electrode structure and partially suppresses crack propagation. In the more detailed view (middle-left), $Li_0PAA\text{-}PEG_{1/10}$ shows some darker spots attributed to polymeric aggregation, which are not visible for most of the other anodes except to a very low extent in the image of Li_0PAA. These aggregates may originate from the more coiled conformation of PAA in acidic form, and it seems that the tendency for this conformation is somehow enhanced by PEGDGE.

In the cross-section images (middle-right), cracks and some horizontal cracks or partial delamination from the current collector can be seen for the acidic PAA-based samples (Li_0PAA and $Li_0PAA\text{-}PEG_{1/10}$), while only smaller cracks are observed for $Li_{0.3}PAA\text{-}PEG_{1/8}$ and almost none for $Li_{0.3}PAA$, $Li_{0.3}PAA\text{-}PEG_{1/10}$, and $Li_{0.3}PAA\text{-}PEG_{1/10@Si}$. When having a closer look, the images of Li_0PAA, $Li_0PAA\text{-}PEG_{1/10}$, and $Li_{0.3}PAA\text{-}PEG_{1/8}$ show even voids within the anode, while for $Li_{0.3}PAA$, $Li_{0.3}PAA\text{-}PEG_{1/10}$, and $Li_{0.3}PAA\text{-}PEG_{1/10@Si}$, the anode is still rather compact and homogeneous. It indicates that even though their surfaces show cracks and therefore degradation, the cross-sections stay in better condition for the $Li_{0.3}PAA$-based modifications. The only exception is $Li_{0.3}PAA\text{-}PEG_{1/8}$, where the higher PEGDGE amount leads to visible voids and interlayer separation, implying that excessive cross-linker incorporation reduces binder flexibility and compromises film adhesion. In the images of $Li_{0.3}PAA\text{-}PEG_{1/10@Si}$, some bright regions between the particles can be observed, possibly corresponding to conductive domains. This might be related to the PEG-functionalization on the Si particles. When looking at the detailed cross-section of the particles (right images), $Li_0PAA\text{-}PEG_{1/10}$ shows low particle degradation and a thin, uniform dark interfacial layer attributed to SEI. The presence of a coherent and continuous SEI film, together with restrained particle degradation, highlights the beneficial role of moderate PEG cross-linking in accommodating Si volume expansion while maintaining electrical connectivity.

In comparison to Li_0PAA, the morphology of $Li_0PAA\text{-}PEG_{1/10}$ shows a notable improvement. In the case of $Li_{0.3}PAA$, the particles seem to be a bit more degraded and have a thick SEI around the particles. Both anodes did not sustain many cycles; therefore, the degradation of particles is rather modest. In contrast, the particles of $Li_{0.3}PAA\text{-}PEG_{1/10}$ show a substantially higher degree of particle degradation accompanied by a porous, moss-like SEI. Interestingly, the particle degradation is much more pronounced than for the sample without PEGDGE ($Li_{0.3}PAA$). In $Li_{0.3}PAA\text{-}PEG_{1/10@Si}$, the particle degradation is again lower, and the surrounding SEI is thinner and more uniform; both seem to be the reason for better cycling performance of this anode compared to the one with $Li_{0.3}PAA\text{-}PEG_{1/10}$.

Further evidence supporting these observations is provided by the high-resolution cross-section SEM–EDX analysis (Figure S8). Interestingly, the EDX elemental mapping of sample $Li_{0.3}PAA\text{-}PEG_{1/10@Si}$ shows that the bright conductive parts between the particles are related to Cu. This could be an indication of a continuous ion-conducting network of PEG around the particles because the copper ions were transported across the electrode from the already known copper carboxylates of PAA at the binder-copper substrate interface.[34]

Finally, XPS was used on the post-mortem electrodes to get a more detailed insight into the degradation products at the surface of the anodes and the influence of PEG cross-linking. The survey spectra of (a) Li_0PAA, (b) Li_0 $PAA\text{-}PEG_{1/10}$, (c) $Li_{0.3}PAA$, (d) $Li_{0.3}PAA\text{-}PEG_{1/10}$, and (e) $Li_{0.3}PAA\text{-}PEG_{1/10@Si}$ are displayed in Figure S9 showing the C 1s and O 1s peaks from binder and electrolyte decomposition products together with F 1s and P 2p peaks from electrolyte decomposition. Only very small Si 2p peaks are visible, most probably due to a rather thick SEI formed during cycling. In the detail spectra in Figure 8, the influence of the anode binder on the electrolyte degradation products can be seen. The Si 2p peaks are mostly comparable between the samples and rather low in intensity due to electrolyte degradation products on the particle surface. The spectra in the C 1s region show peaks related to carbonates and binders, all of them with comparable peak ratios between the samples. Peaks related to C–O (at 533.5 eV) and $C{=}O/PO_4^{3-}$ (at 532 eV)[59] can be discerned in the spectra in the O 1s region, with comparatively lower intensity of C–O for the samples $Li_0PAA\text{-}PEG_{1/10}$ and $Li_{0.3}PAA\text{-}PEG_{1/10}$. In case of $Li_{0.3}PAA\text{-}PEG_{1/10@Si}$, the intensity ratio is similar between both peaks, which could indicate less degradation products as less $C{=}O/PO_4^{3-}$ is observed. According to the F 1s spectra, the amount of residual $LiPF_6$ is highest for Li_0PAA and $Li_{0.3}PAA\text{-}PEG_{1/10}$ and lowest for $Li_{0.3}PAA$. All $Li_{0.3}PAA$-based samples show higher intensities for LiF at 685 eV, which could hint to a higher contribution of inorganic species to the SEI, which is more rigid and stable to avoid further electrolyte decomposition.[65,66] In the P 2p spectra, a lower amount of phosphates can be observed for $Li_{0.3}PAA\text{-}PEG_{1/10@Si}$. Other than that, the spectra are very comparable for all samples. Therefore, the decomposition of the electrolyte seems to happen in a similar way for all the samples, but with higher LiF content in the SEI for $Li_{0.3}PAA\text{-}PEG_{1/10}$ and $Li_{0.3}PAA\text{-}PEG_{1/10@Si}$ and with slightly fewer phosphorous decomposition products for $Li_{0.3}PAA\text{-}PEG_{1/10@Si}$.

■ CONCLUSIONS

In this work, in situ cross-linked binder variations of polyacrylic acid (PAA) with poly(ethylene glycol) diglycidyl ether (PEGDGE) were studied, and their beneficial effect on the mechanical and electrochemical performance of pure Si anodes was demonstrated. The use of partially neutralized PAA facilitates decoiling of the polymer chains and improves cross-linking efficiency with PEGDGE, resulting in increased thermal stability and adhesion. XPS analysis and mechanical tests indicate a higher cross-linking ratio for the $Li_{0.3}PAA$-based anodes, which correlates with improved electrode integrity. Electrochemical analysis reveals that PEGDGE, although added in small quantities, influences the alloying of Si and lithium-ion transport. An optimal PEGDGE-to-PAA ratio of 1:10 yields the most stable cycling performance, with $Li_{0.3}PAA\text{-}PEG_{1/10}$ showing comparable stability to PAA binders and slightly improved rate capability.

In full pouch cells with NMC811 as the cathode, the $Li_{0.3}PAA\text{-}PEG_{1/10@Si}$-containing anode showed a comparable cycle life as $Li_{0.3}PAA$ considering the C/3 check-up cycle, but with stronger 1C degradation, which is nevertheless more linear than for $Li_{0.3}PAA$, which accelerated toward 150 cycles. The $Li_{0.3}PAA\text{-}PEG_{1/10@Si}$ sample maintained its alloying/dealloying mechanisms, as confirmed by post-mortem CV analysis. Also, in the post-mortem SEM-EDX analysis, the $Li_{0.3}PAA\text{-}PEG_{1/10}$ and $Li_{0.3}PAA\text{-}PEG_{1/10@Si}$ anodes showed a well-maintained electrode structure with homogeneous particle degradation. XPS proved that a more inorganic and stable SEI formed on the samples including $Li_{0.3}PAA\text{-}PEG_{1/10}$ and $Li_{0.3}PAA\text{-}PEG_{1/10@Si}$,

Downloaded from pubs.acs.org/aaemcq/article-pdf/9/16/10674/6654359/ae-2026-015488.pdf by KIT BIBLIOTHEK user on 02 November 2026

https://doi.org/10.1021/acsaem.6c01548
ACS Appl. Energy Mater. 2026, 9, 10674−10688

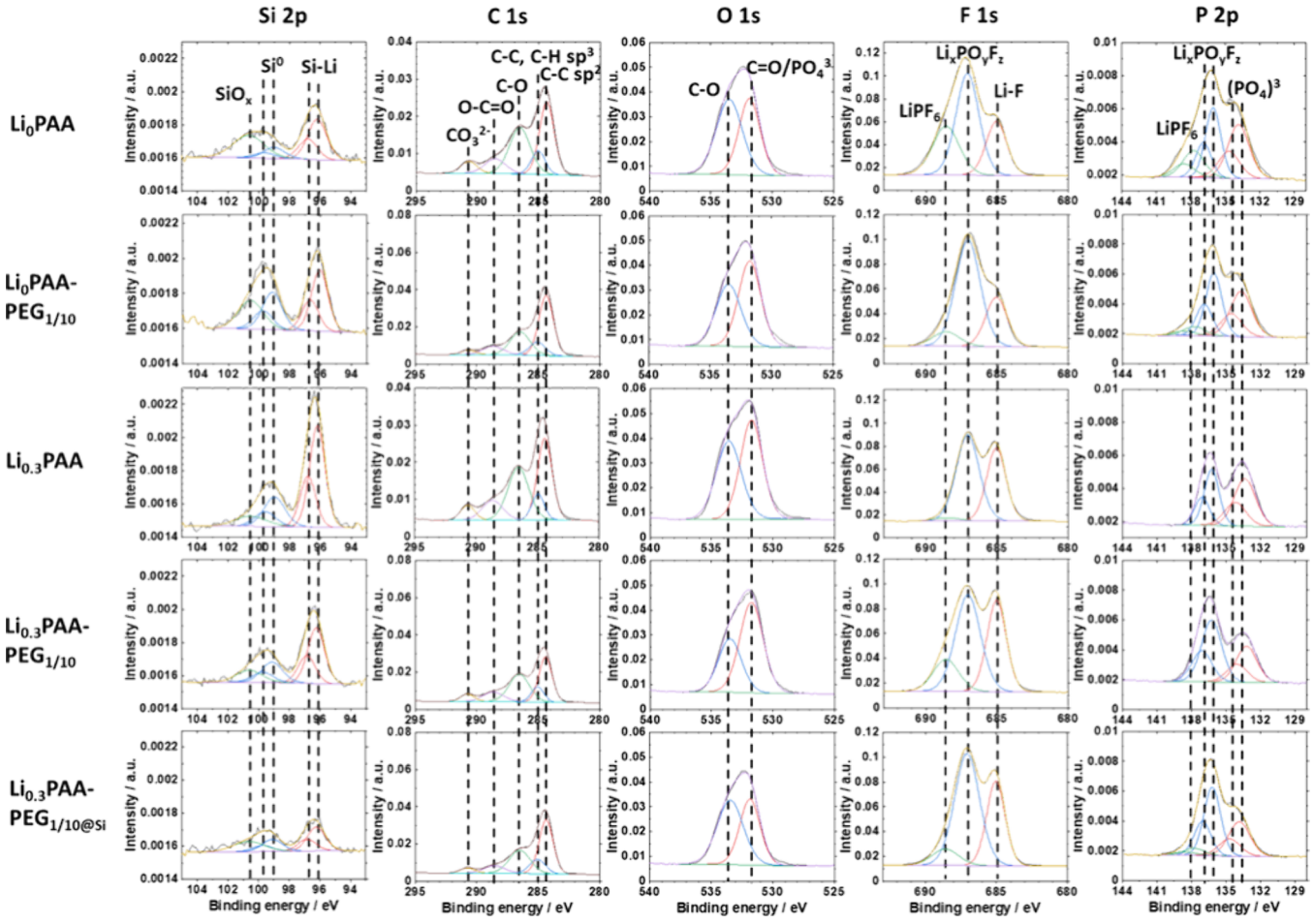


Figure 8. XPS detail measurements in the Si 2p, C 1s, O 1s, F 1s, and P 2p regions from post-mortem electrodes containing Li_0PAA, $Li_0PAA\text{-}PEG_{1/10}$, $Li_{0.3}PAA$, $Li_{0.3}PAA\text{-}PEG_{1/10}$, and $Li_{0.3}PAA\text{-}PEG_{1/10@Si}$ after 1C cycling until SOH = 70–80%.

which is characterized by increased LiF and reduced phosphate content, further supporting the improved long-term performance.

In conclusion, these findings highlight the potential of PEGDGE as a functional cross-linker in Si anodes. It can be introduced easily as an in situ cross-linker for the PAA binder and systematically improves the mechanical integrity, electrode microstructure, interfacial chemistry, and electrochemical performance of the Si-dominant anode. The method of implementation—either via binder modification or Si-particle functionalization—plays a critical role in determining the resulting electrode performance and degradation behavior. Therefore, future work should focus on optimizing the balance between PAA neutralization, PEGDGE content and Si-surface functionalization to tailor binder architecture, electrode integrity, and interfacial stability. Such optimization will be essential for translating cross-linked PAA-PEG binder systems into more durable Si-dominant anodes for Li-ion full cells.

■ ASSOCIATED CONTENT

Supporting Information

The Supporting Information is available free of charge at https://pubs.acs.org/doi/10.1021/acsaem.6c01548.

XPS survey spectra and detail measurements of silicon powder, pure PAA on copper foil, cross-linked PAA-PEG on copper foil, pristine Li_0PAA, $Li_0PAA\text{-}PEG_{1/10}$, $Li_{0.3}PAA$, $Li_{0.3}PAA\text{-}PEG_{1/10}$, and $Li_{0.3}PAA\text{-}PEG_{1/10@Si}$; XPS survey spectra of post-mortem anodes Li_0PAA, $Li_0PAA\text{-}PEG_{1/10}$, $Li_{0.3}PAA$, $Li_{0.3}PAA\text{-}PEG_{1/10}$, and $Li_{0.3}PAA\text{-}PEG_{1/10@Si}$ after 1C cycling until SOH = 70–80%; DSC/TGA data of pure PAA powder, pure PAA cross-linked on polymer foil, pure PEGDGE, cross-linked PAA-PEGDGE, pristine Li_0PAA, $Li_0PAA\text{-}PEG_{1/10}$, $Li_{0.3}PAA\text{-}PEG_{1/10}$, and $Li_{0.3}PAA\text{-}PEG_{1/10@Si}$; SEM-EDX images in top-view and cross-section view of pristine $Li_0PAA\text{-}PEG_{1/10}$, $Li_{0.3}PAA\text{-}PEG_{1/8}$, $Li_{0.3}PAA\text{-}PEG_{1/10}$, and $Li_{0.3}PAA\text{-}PEG_{1/10@Si}$; SEM-EDX images in cross-section view of post-mortem Li_0PAA, $Li_0PAA\text{-}PEG_{1/10}$, $Li_{0.3}PAA$, $Li_{0.3}PAA\text{-}PEG_{1/8}$, $Li_{0.3}PAA\text{-}PEG_{1/10}$, and $Li_{0.3}PAA\text{-}PEG_{1/10@Si}$ anodes after 1C cycling until SOH = 70–80%; and post-mortem cyclic voltammograms of Li_0PAA, $Li_{0.3}PAA$, $Li_0PAA\text{-}PEG_{1/10}$, $Li_{0.3}PAA\text{-}PEG_{1/10}$, and $Li_{0.3}PAA\text{-}PEG_{1/10@Si}$ after 1C cycling until SOH = 70–80% (DOCX)

■ AUTHOR INFORMATION

Corresponding Authors

Gabriele Kloker – *Mercedes-Benz AG, Mercedesstraße 130/6, 70327 Stuttgart, Germany; Institute of Inorganic Chemistry I,*

Downloaded from pubs.acs.org/aaemcq/article-pdf/9/16/10674/6654359/ae-2026-015488.pdf by KIT BIBLIOTHEK user on 02 November 2026

https://doi.org/10.1021/acsaem.6c01548
ACS Appl. Energy Mater. 2026, 9, 10674−10688

Ulm University, Albert-Einstein-Allee 11, 89081 Ulm, Germany; orcid.org/0000-0002-3131-6505; Email: gabriele.kloker@mercedes-benz.com; gabriele.kloker@uni-ulm.de

Montaha Anjass – *Institute of Inorganic Chemistry I, Ulm University, Albert-Einstein-Allee 11, 89081 Ulm, Germany; Department of Chemistry, University of Sharjah, Sharjah 27272, United Arab Emirates;* orcid.org/0000-0002-9197-4526; Email: malmasri@sharjah.ac.ae

Authors

Dragoljub Vrankovic – *Daimler Trucks AG, Fasanenweg 10, 70771 Leinfelden-Echterdingen, Germany*

Nikhil Arya – *Institute of Inorganic Chemistry I, Ulm University, Albert-Einstein-Allee 11, 89081 Ulm, Germany; Helmholtz Institute Ulm (HIU), Helmholtzstr. 11, 89081 Ulm, Germany*

Complete contact information is available at: https://pubs.acs.org/doi/10.1021/acsaem.6c01548

Author Contributions

The manuscript was written through contributions of all authors. All authors have given approval to the final version of the manuscript.

Notes

The authors declare the following competing financial interest(s): G.Kloker has patent # 102025142192.7 pending to Mercedes-Benz Group AG.

■ ACKNOWLEDGMENTS

We acknowledge the financial support of Mercedes-Benz AG (Stuttgart, Germany). M.A. gratefully acknowledges the financial support from the Deutsche Forschungsgemeinschaft (DFG, German Research Foundation) under Germany's Excellence Strategy – EXC 2154 – Project number 390874152 (POLiS Cluster of Excellence). Financial support by Ulm University is gratefully acknowledged. The authors acknowledge Dr. Thomas Diemant (Helmholtz Institute Ulm) for executing and evaluating the XPS measurements. This work contributes to the research performed at CELEST (the Center for Electrochemical Energy Storage Ulm-Karlsruhe).

■ ABBREVIATIONS

ATR	attenuated total reflection
CC	constant current
CCCV	constant current constant voltage
CE	Coulombic efficiency
CV	cyclic voltammetry
DMC	dimethyl carbonate
DSC	differential scanning calorimetry
EC	ethylene carbonate
EMC	ethyl methyl carbonate
EDX	energy-dispersive X-ray spectroscopy
FCE	first cycle efficiency
FEC	fluoroethylene carbonate
FTIR	fourier-transform infrared spectroscopy
Li	Lithium
LIB	Lithium-ion battery
LiOH	lithium hydroxide
Li_xPAA	partially lithiated/neutralized polyacrylic acid
M_w	molecular weight
MWCNT	multi-walled carbon nanotubes
N/P ratio	negative-to-positive ratio
PAA	polyacrylic acid
PEG	polyethylene glycol
PEGDGE	poly(ethylene glycol) diglycidyl ether
PEO	polyethylene oxide
PVDF	polyvinylidene fluoride
ROP	ring-opening polymerization
SEI	solid electrolyte interphase
SEM	scanning electron microscopy
Si	Silicon
SiMP	Silicon microparticles
SiNP	Silicon nanoparticles
SOH	state of health
SiO_x	silicon oxide
SWCNT	single-walled carbon nanotubes
TGA	thermogravimetric analysis
VC	vinylene carbonate
wt %	weight percentages

■ REFERENCES

(1) Obrovac, M. N. Si-alloy negative electrodes for Li-ion batteries. *Curr. Opin. Electrochem.* **2018**, *9*, 8–17.

(2) Feng, K.; Li, M.; Liu, W.; Kashkooli, A. G.; Xiao, X.; Cai, M.; Chen, Z. Silicon-Based Anodes for Lithium-Ion Batteries: From Fundamentals to Practical Applications. *Small* **2018**, *14* (8), 1702737.

(3) Obrovac, M. N.; Chevrier, V. L. Alloy negative electrodes for Li-ion batteries. *Chem. Rev.* **2014**, *114* (23), 11444–11502.

(4) Armand, M.; Axmann, P.; Bresser, D.; Copley, M.; Edström, K.; Ekberg, C.; Guyomard, D.; Lestriez, B.; Novák, P.; Petranikova, M.; Porcher, W.; Trabesinger, S.; Wohlfahrt-Mehrens, M.; Zhang, H. Lithium-ion batteries – Current state of the art and anticipated developments. *J. Power Sources* **2020**, *479*, 228708.

(5) Zuo, X.; Zhu, J.; Müller-Buschbaum, P.; Cheng, Y.-J. Silicon based lithium-ion battery anodes: A chronicle perspective review. *Nano Energy* **2017**, *31*, 113–143.

(6) Zhang, C.; Wang, F.; Han, J.; Bai, S.; Tan, J.; Liu, J.; Li, F. Challenges and Recent Progress on Silicon-Based Anode Materials for Next-Generation Lithium-Ion Batteries. *Small Struct.* **2021**, *2* (6), 2100009.

(7) Gopinadh, S. V.; Phanendra, P. V. R. L.; V, A.; John, B.; T. D., M. Progress, Challenges, and Perspectives on Alloy-Based Anode Materials for Lithium Ion Battery: A Mini-Review. *Energy Fuels* **2024**, *38* (18), 17253–17277.

(8) Zhu, B.; Liu, G.; Lv, G.; Mu, Y.; Zhao, Y.; Wang, Y.; Li, X.; Yao, P.; Deng, Y.; Cui, Y.; Zhu, J. Minimized lithium trapping by isovalent isomorphism for high initial Coulombic efficiency of silicon anodes. *Sci. Adv.* **2019**, *5* (11), eaax0651.

(9) Li, Y.; Zheng, X.; Cao, Z.; Wang, Y.; Wang, Y.; Lv, L.; Huang, W.; Huang, Y.; Zheng, H. Unveiling the mechanisms into Li-trapping induced (ir)reversible capacity loss for silicon anode. *Energy Storage Mater.* **2023**, *55*, 660–668.

(10) Rehnlund, D.; Lindgren, F.; Böhme, S.; Nordh, T.; Zou, Y.; Pettersson, J.; Bexell, U.; Boman, M.; Edström, K.; Nyholm, L. Lithium trapping in alloy forming electrodes and current collectors for lithium based batteries. *Energy Environ. Sci.* **2017**, *10* (6), 1350–1357.

(11) Su, X.; Wu, Q.; Li, J.; Xiao, X.; Lott, A.; Lu, W.; Sheldon, B. W.; Wu, J. Silicon-Based Nanomaterials for Lithium-Ion Batteries: A Review. *Adv. Energy Mater.* **2014**, *4* (1), 1300882.

(12) Eshetu, G. G.; Zhang, H.; Judez, X.; Adenusi, H.; Armand, M.; Passerini, S.; Figgemeier, E. Production of high-energy Li-ion batteries

Downloaded from pubs.acs.org/aaemcq/article-pdf/9/16/10674/6654359/ae-2026-015488.pdf by KIT BIBLIOTHEK user on 02 November 2026

comprising silicon-containing anodes and insertion-type cathodes. *Nat. Commun.* **2021**, *12* (1), 5459.
(13) Li, F.; Xu, J.; Hou, Z.; Li, M.; Yang, R. Silicon Anodes for High-Performance Storage Devices: Structural Design, Material Compounding, Advances in Electrolytes and Binders. *ChemNanoMat* **2020**, *6* (5), 720–738.
(14) Lee, J. K.; Oh, C.; Kim, N.; Hwang, J.-Y.; Sun, Y.-K. Rational design of silicon-based composites for high-energy storage devices. *J. Mater. Chem. A* **2016**, *4* (15), 5366–5384.
(15) Wu, H.; Cui, Y. Designing nanostructured Si anodes for high energy lithium ion batteries. *Nano Today* **2012**, *7* (5), 414–429.
(16) Zhao, X.; Lehto, V.-P. Challenges and prospects of nanosized silicon anodes in lithium-ion batteries. *Nanotechnology* **2021**, *32* (4), 42002.
(17) Yang, Y.; Yuan, W.; Kang, W.; Ye, Y.; Yuan, Y.; Qiu, Z.; Wang, C.; Zhang, X.; Ke, Y.; Tang, Y. Silicon-nanoparticle-based composites for advanced lithium-ion battery anodes. *Nanoscale* **2020**, *12* (14), 7461–7484.
(18) Liu, X. H.; Zhong, L.; Huang, S.; Mao, S. X.; Zhu, T.; Huang, J. Y. Size-dependent fracture of silicon nanoparticles during lithiation. *ACS Nano* **2012**, *6* (2), 1522–1531.
(19) Zhu, G.; Chao, D.; Xu, W.; Wu, M.; Zhang, H. Microscale Silicon-Based Anodes: Fundamental Understanding and Industrial Prospects for Practical High-Energy Lithium-Ion Batteries. *ACS Nano* **2021**, *15* (10), 15567–15593.
(20) Obrovac, M. N.; Christensen, L.; Le, D. B.; Dahn, J. R. Alloy Design for Lithium-Ion Battery Anodes. *J. Electrochem. Soc.* **2007**, *154* (9), A849.
(21) Wang, H.; Wu, B.; Wu, X.; Zhuang, Q.; Liu, T.; Pan, Y.; Shi, G.; Yi, H.; Xiong, Z.; Chou, S.-L.; Wang, B. Key Factors for Binders to Enhance the Electrochemical Performance of Silicon Anodes through Molecular Design. *Small* **2022**, *18* (18), 2101680.
(22) Chen, H.; Ling, M.; Hencz, L.; Ling, H. Y.; Li, G.; Lin, Z.; Liu, G.; Zhang, S. Exploring Chemical, Mechanical, and Electrical Functionalities of Binders for Advanced Energy-Storage Devices. *Chem. Rev.* **2018**, *118* (18), 8936–8982.
(23) Choi, S.; Kwon, T.-W.; Coskun, A.; Choi, J. W. Highly elastic binders integrating polyrotaxanes for silicon microparticle anodes in lithium ion batteries. *Science* **2017**, *357* (6348), 279–283.
(24) Miranda, A.; Sarang, K.; Gendensuren, B.; Oh, E.-S.; Lutkenhaus, J.; Verduzco, R. Molecular design principles for polymeric binders in silicon anodes. *Mol. Syst. Des. Eng.* **2020**, *5* (4), 709–724.
(25) Munaoka, T.; Yan, X.; Lopez, J.; To, J. W. F.; Park, J.; Tok, J. B.-H.; Cui, Y.; Bao, Z. Ionically Conductive Self-Healing Binder for Low Cost Si Microparticles Anodes in Li-Ion Batteries. *Adv. Energy Mater.* **2018**, *8* (14), 1703138.
(26) Xu, Z.; Yang, J.; Zhang, T.; Nuli, Y.; Wang, J.; Hirano, S. Silicon Microparticle Anodes with Self-Healing Multiple Network Binder. *Joule* **2018**, *2* (5), 950–961.
(27) Zhao, Y.-M.; Yue, F.-S.; Li, S.-C.; Zhang, Y.; Tian, Z.-R.; Xu, Q.; Xin, S.; Guo, Y.-G. Advances of polymer binders for silicon-based anodes in high energy density lithium-ion batteries. *InfoMat* **2021**, *3* (5), 460–501.
(28) Preman, A. N.; Lee, H.; Yoo, J.; Kim, I. T.; Saito, T.; Ahn, S. Progress of 3D network binders in silicon anodes for lithium ion batteries. *J. Mater. Chem. A* **2020**, *8* (48), 25548–25570.
(29) Salini, P. S.; Gopinadh, S. V.; Kalpakasseri, A.; John, B.; Thelakkattu Devassy, M. Toward Greener and Sustainable Li-Ion Cells: An Overview of Aqueous-Based Binder Systems. *ACS Sustainable Chem. Eng.* **2020**, *8* (10), 4003–4025.
(30) Zou, F.; Manthiram, A. A Review of the Design of Advanced Binders for High-Performance Batteries. *Adv. Energy Mater.* **2020**, *10* (45), 2002508.
(31) Eshetu, G. G.; Figgemeier, E. Confronting the Challenges of Next-Generation Silicon Anode-Based Lithium-Ion Batteries: Role of Designer Electrolyte Additives and Polymeric Binders. *ChemSusChem* **2019**, *12* (12), 2515–2539.
(32) Li, J.-T.; Wu, Z.-Y.; Lu, Y.-Q.; Zhou, Y.; Huang, Q.-S.; Huang, L.; Sun, S.-G. Water Soluble Binder, an Electrochemical Performance Booster for Electrode Materials with High Energy Density. *Adv. Energy Mater.* **2017**, *7* (24), 1701185.
(33) Bresser, D.; Buchholz, D.; Moretti, A.; Varzi, A.; Passerini, S. Alternative binders for sustainable electrochemical energy storage – the transition to aqueous electrode processing and bio-derived polymers. *Energy Environ. Sci.* **2018**, *11* (11), 3096–3127.
(34) Xiong, J.; Dupré, N.; Mazouzi, D.; Guyomard, D.; Roué, L.; Lestriez, B. Influence of the Polyacrylic Acid Binder Neutralization Degree on the Initial Electrochemical Behavior of a Silicon/Graphite Electrode. *ACS Appl. Mater. Interfaces* **2021**, *13* (24), 28304–28323.
(35) Hays, K. A.; Ruther, R. E.; Kukay, A. J.; Cao, P.; Saito, T.; Wood, D. L.; Li, J. What makes lithium substituted polyacrylic acid a better binder than polyacrylic acid for silicon-graphite composite anodes?. *J. Power Sources* **2018**, *384*, 136–144.
(36) Li, Z.; Tang, W.; Yang, Y.; Lai, G.; Lin, Z.; Xiao, H.; Qiu, J.; Wei, X.; Wu, S.; Lin, Z. Engineering Prelithiation of Polyacrylic Acid Binder: A Universal Strategy to Boost Initial Coulombic Efficiency for High-Areal-Capacity Si-Based Anodes. *Adv. Funct. Mater.* **2022**, *32* (40), 2206615.
(37) Dang, D.; Wang, Y.; Wang, M.; Hu, J.; Ban, C.; Cheng, Y.-T. Lithium Substituted Poly(acrylic acid) as a Mechanically Robust Binder for Low-Cost Silicon Microparticle Electrodes. *ACS Appl. Energy Mater.* **2020**, *3* (11), 10940–10949.
(38) Kloker, G.; Vrankovic, D.; Arya, N.; Diemant, T.; Anjass, M. Enabling Si-Dominant Anodes: Influence of Neutralization Degree of Polyacrylic Acid on Low-Cost Micron-Sized Silicon Anode in High-Energy Li-Ion Full Cell. *Batteries Supercaps* **2024**, *7*, e202400330.
(39) Martin, T. R.; Pekarek, R. T.; Coyle, J. E.; Schulze, M. C.; Neale, N. R. Understanding why poly(acrylic acid) works: decarbonylation and cross-linking provide an ionically conductive passivation layer in silicon anodes. *J. Mater. Chem. A* **2021**, *9* (38), 21929–21938.
(40) Samridh, A.; Gopinadh, S. V.; John, B.; Sarojiniamma, S.; Devassia, M. T.; Joseph, M. G. Sustainable Binder System: Cross-Linked Tamarind Gum-Polyacrylic Acid for Silicon-Graphite Anodes in Future Lithium-Ion Batteries. *Energy Technol.* **2025**, *13* (5), 2401837.
(41) Samridh, A.; Gopinadh, S. V.; John, B.; Phanindra, P. V. R. L.; Mary Gladis, J.; Sujatha, S.; Mercy, T. D. Cross-linked carboxymethyl cellulose–polyacrylic acid as a binder for thermally treated silicon–graphite@graphite based anodes: a multipronged approach towards realising silicon–graphite based anodes for lithium-ion cells. *RSC Sustain.* **2025**, *3* (11), 5333–5345.
(42) Mazouzi, D.; Karkar, Z.; Reale Hernandez, C.; Jimenez Manero, P.; Guyomard, D.; Roué, L.; Lestriez, B. Critical roles of binders and formulation at multiscales of silicon-based composite electrodes. *J. Power Sources* **2015**, *280*, 533–549.
(43) Zhu, W.; Zhou, J.; Xiang, S.; Bian, X.; Yin, J.; Jiang, J.; Yang, L. Progress of Binder Structures in Silicon-Based Anodes for Advanced Lithium-Ion Batteries: A Mini Review. *Front. Chem.* **2021**, *9*, 712225.
(44) Park, S.; Kim, S.; Lee, J.-A.; Ue, M.; Choi, N.-S. Liquid electrolyte chemistries for solid electrolyte interphase construction on silicon and lithium-metal anodes. *Chem. Sci.* **2023**, *14* (37), 9996–10024.
(45) Song, Z.; Chen, F.; Martinez-Ibañez, M.; Feng, W.; Forsyth, M.; Zhou, Z.; Armand, M.; Zhang, H. A reflection on polymer electrolytes for solid-state lithium metal batteries. *Nat. Commun.* **2023**, *14* (1), 4884.
(46) Nam, J.; Kim, E.; K K, R.; Kim, Y.; Kim, T.-H. A conductive self healing polymeric binder using hydrogen bonding for Si anodes in lithium ion batteries. *Sci. Rep.* **2020**, *10* (1), 14966.
(47) Jiang, S.; Hu, B.; Sahore, R.; Liu, H.; Pach, G. F.; Carroll, G. M.; Zhang, L.; Zhao, B.; Neale, N. R.; Zhang, Z. Tailoring the Surface of Silicon Nanoparticles for Enhanced Chemical and Electrochemical Stability for Li-Ion Batteries. *ACS Appl. Energy Mater.* **2019**, *2* (9), 6176–6183.
(48) Gonzalez, M.; Minnici, K.; Risteen, B.; Wang, L.; Housel, L. M.; Renderos, G. D.; Takeuchi, K. J.; Takeuchi, E. S.; Marschilok, A. C.; Fuller, T. F.; Reichmanis, E. Active Material Interfacial Chemistry and Its Impact on Composite Magnetite Electrodes. *ACS Appl. Energy Mater.* **2021**, *4* (9), 9836–9847.

Downloaded from pubs.acs.org/aaemcq/article-pdf/9/16/10674/6654359/ae-2026-015488.pdf by KIT BIBLIOTHEK user on 02 November 2026

https://doi.org/10.1021/acsaem.6c01548
ACS Appl. Energy Mater. 2026, 9, 10674–10688

(49) Kloker, G.; Pervez, S. A.; Hoefling, A.; Fichtner, M. Improving the Electrochemical Properties of Advanced Cross-Linked Solid Polymer Composite Electrolytes. *ACS Appl. Energy Mater.* **2022**, *5* (11), 13410–13418.
(50) Nair, J. R.; Shaji, I.; Ehteshami, N.; Thum, A.; Diddens, D.; Heuer, A.; Winter, M. Solid Polymer Electrolytes for Lithium Metal Battery via Thermally Induced Cationic Ring-Opening Polymerization (CROP) with an Insight into the Reaction Mechanism. *Chem. Mater.* **2019**, *31* (9), 3118–3133.
(51) Tran, B.; Oladeji, I. O.; Wang, Z.; Calderon, J.; Chai, G.; Atherton, D.; Zhai, L. Adhesive PEG-based binder for aqueous fabrication of thick $Li_4Ti_5O_{12}$ electrode. *Electrochim. Acta* **2013**, *88*, 536–542.
(52) Teng, X.; Xu, H.; Song, W.; Shi, J.; Xin, J.; Hiscox, W. C.; Zhang, J. Preparation and Properties of Hydrogels Based on PEGylated Lignosulfonate Amine. *ACS Omega* **2017**, *2* (1), 251–259.
(53) Moharram, M. A.; Khafagi, M. G. Thermal behavior of poly(acrylic acid)–poly(vinyl pyrrolidone) and poly(acrylic acid)–metal–poly(vinyl pyrrolidone) complexes. *J. Appl. Polym. Sci.* **2006**, *102*, 4049–4057.
(54) Kwon, S. K.; Kim, D. Effect of Process Parameters of UV-Assisted Gas-Phase Cleaning on the Removal of PEG (Polyethyleneglycol) from a Si Substrate. *J. Korean Phys. Soc.* **2006**, *49*, 1421–1427.
(55) Cui, Y.; Liang, X.; Chai, J.; Cui, Z.; Wang, Q.; He, W.; Liu, X.; Liu, Z.; Cui, G.; Feng, J. High Performance Solid Polymer Electrolytes for Rechargeable Batteries: A Self-Catalyzed Strategy toward Facile Synthesis. *Adv. Sci.* **2017**, *4* (11), 1700174.
(56) Haro, J. C. D.; Tatsi, E.; Fagiolari, L.; Bonomo, M.; Barolo, C.; Turri, S.; Bella, F.; Griffini, G. Lignin-Based Polymer Electrolyte Membranes for Sustainable Aqueous Dye-Sensitized Solar Cells. *ACS Sustain. Chem. Eng.* **2021**, *9* (25), 8550–8560.
(57) Eisenberg, A.; Yokoyama, T.; Sambalido, E. Dehydration kinetics and glass transition of poly(acrylic acid). *J. Polym. Sci.* **1969**, *7*, 1717–1728.
(58) Maurer, J. J.; Eustace, D. J.; Ratcliffe, C. T. Thermal characterization of poly(acrylic acid). *Macromolecules* **1987**, *20*, 196–202.
(59) Wu, Z.-Y.; Deng, L.; Li, J.-T.; Zanna, S.; Seyeux, A.; Huang, L.; Sun, S.-G.; Marcus, P.; Światowska, J. Solid Electrolyte Interphase Layer Formation on the Si-Based Electrodes with and without Binder Studied by XPS and ToF-SIMS Analysis. *Batteries* **2022**, *8* (12), 271.
(60) Burdette-Trofimov, M. K.; Armstrong, B. L.; Rogers, A. M.; Heroux, L.; Doucet, M.; Yang, G.; Phillip, N. D.; Kidder, M. K.; Veith, G. M. Understanding Binder–Silicon Interactions during Slurry Processing. *J. Phys. Chem. C* **2020**, *124* (24), 13479–13494.
(61) Wang, M.-S.; Fan, L.-Z. Silicon/carbon nanocomposite pyrolyzed from phenolic resin as anode materials for lithium-ion batteries. *J. Power Sources* **2013**, *244*, 570–574.
(62) Datta, M. K.; Kumta, P. N. In situ electrochemical synthesis of lithiated silicon-carbon based composites anode materials for lithium ion batteries. *J. Power Sources* **2009**, *194*, 1043–1052.
(63) Obrovac, M. N.; Krause, L. Reversible Cycling of Crystalline Silicon Powder. *J. Electrochem. Soc.* **2007**, *154*, A103–A108.
(64) Reyes Jiménez, A.; Klöpsch, R.; Wagner, R.; Rodehorst, U. C.; Kolek, M.; Nölle, R.; Winter, M.; Placke, T. A Step toward High-Energy Silicon-Based Thin Film Lithium Ion Batteries. *ACS Nano* **2017**, *11* (5), 4731–4744.
(65) Jia, T.; Zhong, G.; Lu, S.; Ren, X.; Lv, Y.; Li, N.; Yin, R.; Kang, G.; Cai, K.; Kang, F.; Cao, Y. Interfacial fluoride engineering enabled robust LiF-rich solid electrolyte interphase to reduce active lithium loss in rechargeable lithium battery. *Chem. Eng. J.* **2023**, *454*, 140397.
(66) Parikh, P.; Sina, M.; Banerjee, A.; Wang, X.; D'Souza, M. S.; Doux, J.-M.; Wu, E. A.; Trieu, O. Y.; Gong, Y.; Zhou, Q.; Snyder, K.; Meng, Y. S. Role of Polyacrylic Acid (PAA) Binder on the Solid Electrolyte Interphase in Silicon Anodes. *Chem. Mater.* **2019**, *31* (7), 2535–2544.

Downloaded from pubs.acs.org/aaemcq/article-pdf/9/16/10674/6654359/ae-2026-015488.pdf by KIT BIBLIOTHEK user on 02 November 2026

https://doi.org/10.1021/acsaem.6c01548
ACS Appl. Energy Mater. 2026, 9, 10674–10688